

P-38

Final Technical Report

NASA Award No. NAG-1-868

Lidar Cloud Studies for FIRE and ECLIPS

Submitted by

Kenneth Sassen

Department of Meteorology  
University of Utah  
Salt Lake City, UT 84112

6 August 1990

(NASA-CR-186004) LIDAR CLOUD STUDIES FOR  
FIRE AND ECLIPS Final Report (Utah Univ.)  
38 p. CSCL 04A

NSO-20214

unclas  
63/46 0297559

## Preface

The following report represents an article that has been accepted for publication in the upcoming special topic issue of The Monthly Weather Review, which deals with the 27-28 October 1986 cirrus cloud case study from the Wisconsin IFO campaign. It is a unique work that incorporates findings from five diverse lidar research groups, and I thank my coauthors, Chris Grund, Jim Spinhirne, Mike Hardesty, and Joe Alvarez, for their important contributions. Although the various lidar observations were not spatially consistent (with the exception of some airborne lidar overflight support), the analysis of this extended case study reveals the utility of multiple lidar probing for evaluating a wide range of the characteristics of cirrus cloud systems. We are gratified that the design of the upcoming 1991 FIRE IFO-II experiment will allow a diverse group of lidar, radar, and passive remote sensing systems to be colocated at a central hub site, so as to fully exploit the indicated advantages of the multiple remote sensor approach.

THE 27-28 OCTOBER 1986 FIRE IFO CIRRUS CASE STUDY:  
A FIVE LIDAR OVERVIEW OF CLOUD STRUCTURE AND EVOLUTION

by

Kenneth Sassen,<sup>1</sup> Christian J. Grund,<sup>2</sup> James Spinhirne,<sup>3</sup>

Michael Hardesty<sup>4</sup> and Jose M. Alvarez<sup>5</sup>

ABSTRACT

Optical remote sensing measurements of cirrus cloud properties were collected by one airborne and four ground-based lidar systems over a 32-h period during this case study from the First ISCCP (International Satellite Cloud Climatology Program) Regional Experiment (FIRE) Intensive Field Observation (IFO) program. The lidar systems were variously equipped to collect linear depolarization, intrinsically calibrated backscatter, and Doppler velocity information. Data presented here describe the temporal evolution and spatial distribution of cirrus clouds over an area encompassing southern and central Wisconsin. The cirrus cloud types include: a) dissipating subvisual and "thin" fibrous cirrus cloud bands, b) an isolated mesoscale uncinus complex (MUC), c) a large-scale, deep cloud that developed into an organized cirrus structure within the lidar array, and d) a series of intensifying mesoscale cirrus cloud masses. Although the cirrus frequently developed in the vertical from particle fall-streaks emanating from generating regions at or near cloud tops, glaciating supercooled ( $-30^{\circ}$  to  $-35^{\circ}\text{C}$ ) altocumulus clouds contributed to the production of ice mass at the base of the deep cirrus cloud, apparently even through riming, and other mechanisms involving evaporation, wave motions, and radiative effects are indicated. The generating regions ranged in scale from  $\sim 1.0\text{-km}$  cirrus uncinus cells, to organized MUC structures up to  $\sim 120\text{-km}$  across.

---

<sup>1</sup>Department of Meteorology, University of Utah, Salt Lake City, UT 84112

<sup>2</sup>Department of Meteorology, University of Wisconsin-Madison, Madison, WI 53706

<sup>3</sup>Environmental Sensors Branch, NASA Goddard Space Flight Center, Greenbelt, MD 20771

<sup>4</sup>Atmospheric Lidar Program, Wave Propagation Laboratory, NOAA Environmental Research Laboratories, Boulder, CO 80303

<sup>5</sup>NASA Langley Research Center, Hampton, VA 23665

## 1. Introduction

The design of the 1986 Wisconsin FIRE Intensive Field Observation experiment placed strong emphasis on the collection of ground-based and airborne lidar data of the cirrus clouds within the project study area (see Starr and Wiley 1990, for a project overview). Indeed, although the significant contributions provided by the project aircraft and passive remote sensing stations should not be minimized, this field study can be fundamentally viewed as a lidar cloud experiment, just as other projects have relied chiefly on arrays of microwave radars. As such, this field study represents the first true lidar experiment undertaken with multiple lidars offering a variety of measurement techniques. The lidar sites served as hubs for special rawinsonde releases, radiometric observations, and, when cirrus were present, aircraft operations. Research aircraft from NCAR filed flight patterns based on the availability of satellite and lidar data, and operations in the vicinities of the lidar sites were often guided through ground-to-air communications.

Of the five lidar systems that participated in the field experiment, one was airborne, three collected linear depolarization data, and one each obtained Dopplerized information and direct measurements of cloud backscatter coefficients through a high spectral resolution technique. The various lidar systems were provided by the Universities of Utah and Wisconsin-Madison, NASA, and NOAA. The reliance on these relatively new instruments as a key element to help fulfill the project goals is in keeping with the demonstrated abilities of lidar remote sensing for inferring the physical and radiative properties of cirrus clouds (for a recent summary, see Platt et al. 1987). Unlike the optically denser water, mixed-phase, or ice clouds of the lower and middle troposphere, cirrus clouds are normally rather transparent to lidar probing, although optical attenuation and multiple scattering are always undesirable factors in attempting to derive quantitative information from backscattered laser power using standard techniques. Nonetheless, the great spatial resolution and sensitivity of lidar probing to cirrus clouds provide a powerful tool for determining cloud height, depth, and internal structure. If linear depolarization data are also collected, information on cloud particle phase, shape, and orientation can be inferred. Polarization lidar studies of cirrus from the ground (Sassen et al. 1989a) and high flying aircraft (Spinhirne et al. 1983) have amply illustrated these capabilities. Moreover, as explored for the first time in this paper, lidar determinations of the backscatter phase function also provide information on the shape, and hence phase, of cirrus cloud particles.

In this paper are presented the ensemble of lidar observations corresponding to the FIRE IFO case study period considered in the several companion papers. The data commence at 1600 (all times are UTC) on 27 October 1986, as subvisual and thin cirrus clouds began invading the project area, and end at 2359 on 28 October, as project operations were halted. Our discussion begins with the specifications of the individual lidars and their data gathering abilities, and the general layout of the lidar ground site array and selected airborne lidar flight tracks. Two important overviews of the data collected over the 32-h period are presented. The first is a composite of height-versus-time cloud displays from all four ground-based lidars, which, in combination with rawinsonde data, provides a unique image of the passage of cirrus over a geographical area encompassing central and southern Wisconsin. The second overview involves downward-looking airborne lidar data, which provide an essentially Eulerian view of the cirrus selected from two research missions

flown during the period. Special datasets then highlight findings concerning cloud structure from each lidar system. This contribution to the FIRE IFO case study concludes with an assessment of the cirrus structural changes, and the formation mechanisms and physical scales they imply, over the study period.

## 2. Data Collection

The diamond-shaped array of the four ground-based lidar systems across central and southern Wisconsin is depicted in Fig. 1. The siting of each lidar, in a clockwise fashion starting from Wausau, corresponds to the University of Utah Mobile Polarization Lidar (MPL), the NOAA Wave Propagation Laboratory Doppler Lidar (WPLDL), the University of Wisconsin at Madison High Spectral Resolution Lidar (HSRL), and the NASA Langley Research Center Fourteen-Inch Lidar System (LaRCFILS), respectively. Also given in Fig. 1 are selected flight tracks of the NASA ER-2 aircraft, the platform of the downward-pointing Cloud and Aerosol Lidar System (CALS), for 27 and 28 October. Each flight track is identified by the daily mission leg number, with the arrows indicating the aircraft headings. Below, the characteristics and data quantities retrieved from each lidar system, whose general specifications are compared in Table 1, are briefly described.

### a. The Mobile Polarization Lidar

The MPL consists of a relatively high power, but low pulse repetition rate, ruby laser, and a telescope receiver with dual photomultiplier tubes (PMT) for polarization studies. These components are mounted within a manually steerable yoke inside a compact van for mobile deployment. A microcomputer-based system controls laser operation and the simultaneous two-channel data digitizer. All laser return and supporting data are stored to disk in the field for later transfer to magnetic tape.

The MPL data quantities are the lidar linear depolarization ratio  $\delta$  and the relative returned (parallel-polarized) laser power  $P$ . The two receiver channels, which are polarized parallel ( $\parallel$ ) and orthogonal ( $\perp$ ) to the vertically polarized laser source, are calibrated with respect to one another, such that  $\delta = P_{\perp} / P_{\parallel}$ . Profiles of relative returned laser power are converted into estimates of the volume backscatter coefficient  $\beta_{\pi}$  ( $\text{km sr}^{-1}$ ) on the basis of periodic system calibrations using clear-air returns collected from the upper troposphere (see Sassen et al. 1989b), but it is difficult to accurately correct  $\beta_{\pi}$  values for the effects of laser pulse attenuation lacking additional information (see Platt 1979).

During the 27-28 October case study period, vertically pointing lidar data were collected primarily at a rate of one shot every two minutes. Wausau observations commenced at 1500 with hourly observations, but from ~1800 to 2230 on 27 October data were collected continuously as thin cirrus clouds made their initial appearance and then quickly moved through the area. Operations could not be resumed on the morning of 28 October until ~1430 due to fog in the river valley where the lidar was situated. Although observations continued until 2130, by 1930 stratocumulus clouds began advecting into the area and increasingly disrupted the lidar cirrus cloud measurements.

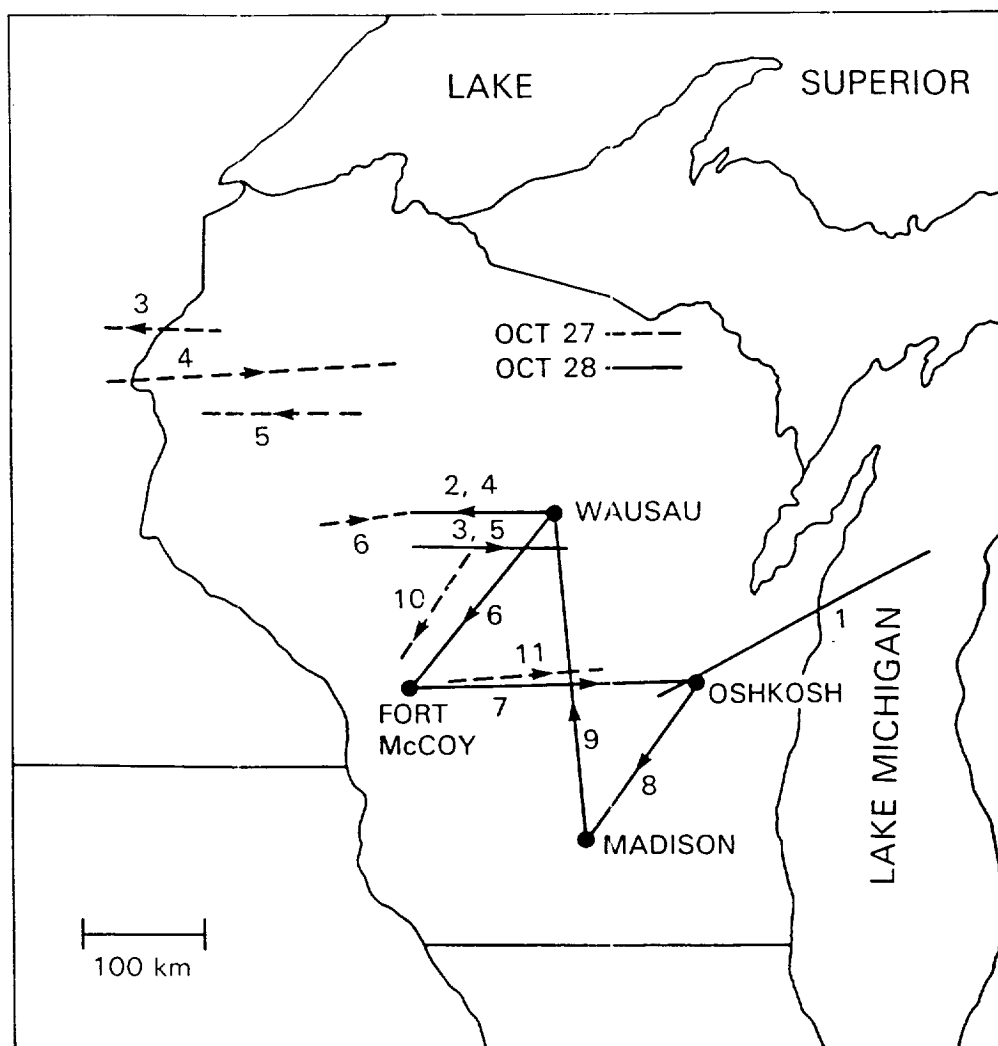


Fig. 1 Map of the Wisconsin FIRE IFO project area showing the diamond-shaped ground-based lidar array, and selected ER-2 airborne lidar flight tracks on 27 October (dashed lines) and 28 October (solid lines).

Table 1 Specifications of the five FIRE IFO lidar systems, as used during the experiment. The various data quantities are defined in Section 2a-e; v and h refer to vertical and horizontal polarizations.

|                               | U. of Utah<br>MPL | NOAA<br>WPLDL            | U. of<br>Wisconsin<br>HSRL                                 | NASA<br>LaRCFILS | NASA<br>CALS |
|-------------------------------|-------------------|--------------------------|--|------------------|--------------|
| <u>FIRE IFO Site</u>          | Wausau            | Oshkosh                  | Madison  | Ft. McCoy        | Airborne     |
| <u>Transmitter</u>            |                   |                          |  |                  |              |
| Laser type                    | Ruby              | CO <sub>2</sub>          | CuCl <sub>2</sub>  | NdYAG            | NdYAG        |
| Wavelength (μm)               | 0.694             | 10.6                     | 0.5106   | 0.532            | 0.532        |
| Peak energy (J)               | 1.5               | 1.0                      | 6.3x10 <sup>-3</sup>                                       | 0.2              | 0.04         |
| Pulse length (ns)             | 30                | 2.0x10 <sup>3</sup>      | 15   | 10               | 5.0          |
| PRF (Hz)                      | 0.25              | 10                       | 8.0x10 <sup>3</sup>  | 20               | 5.0          |
| Beamwidth (mrad)              | 1.0               | 0.05                     | 0.1  | 1.0              | 1.0          |
| Polarization                  | v                 | h                        | --   | v                | v            |
| <u>Receiver</u>               |                   |                          |  |                  |              |
| Diameter (m)                  | 0.25              | 0.28                     | 0.35   | 0.36             | 0.15         |
| Beamwidth (mrad)              | 3.0               | 0.05                     | 0.32   | 2.0              | 1.4          |
| Polarization                  | v + h             | h                        | --   | v + h            | v + h        |
| Detectors                     | PMT,2             | PD                       | PMT,2  | PMT,3            | PMT,2        |
| Scanning (° s <sup>-1</sup> ) | (Manual)          | 30                       | 15   | 10               | (Fixed)      |
| <u>Data Handling</u>          |                   |                          |  |                  |              |
| Range resolution (m)*         | 7.5               | 300                      | 60   | 37.5             | 7.5          |
| Number of channels            | 2                 | 1                        | 2  | 2                | 2            |
| Samples per channel           | 2048              | 100                      | 256  | 2048             | 3072         |
| Pulses averaged               | 1                 | 1-10                     | 3.2x10 <sup>4</sup>  | 1-10             | 1            |
| Data quantities               | P, δ              | P, β <sub>π</sub> ,<br>V | β <sub>π</sub> , β <sub>E</sub> ,<br>P <sub>π</sub> /4π, τ | P, δ             | P, δ         |

\*Effective minimum resolution.

## b. The Wave Propagation Laboratory Doppler Lidar

The basic operating principles of this system differ from those of the other lidars in that it was designed primarily for measurement of wind velocities. In the WPLDL system, backscattered laser radiation is analyzed to yield information on signal intensity, mean frequency, and spectral width. These data are displayed in real time in the lidar van by means of a microcomputer-controlled color display system, and stored on magnetic tape.

To produce the narrow laser pulse frequency bandwidth needed for Doppler wind speed measurement, the WPLDL system incorporates an injection-stabilized pulsed carbon dioxide laser transmitter. At the  $\text{CO}_2$  wavelength, the system detects large aerosol particles ( $>1 \mu\text{m}$  diameter), but is insensitive to molecular scatter. By operating within the atmospheric thermal window, derived data quantities do not have to be extrapolated to obtain thermal infrared properties. The diffraction-limited field-of-view of  $\sim 50 \mu\text{rad}$  effectively eliminates the effects of multiple scattering, which hinders absolute backscatter measurements in dense media such as clouds. As a consequence of the narrowband laser output, however, the transmitted pulse of  $2 \mu\text{s}$  duration yields a range resolution of  $300 \text{ m}$ . Backscattered signals are detected at this wavelength using a photodiode (PD).

The transmitted beam can be scanned hemispherically by means of a computer controller. During the case study period, data were gathered in three different scan modes. Velocity-azimuth display (VAD) scans at fixed elevation angles, and range-height indicator (RHI) scans (from  $0^\circ$  to  $180^\circ$ ) along selected azimuth angles provided information on wind profiles and cirrus spatial structure. These scans were interleaved with vertically pointing data collected at a  $1\text{--}10 \text{ s}^{-1}$  pulse rate to study cirrus vertical structure. Each zenith data file was averaged for computation of calibrated mean backscatter coefficient profiles using the BETA program (Post 1984). Note that since the single-shot Doppler velocity accuracy is  $\sim 0.8 \text{ m s}^{-1}$ , comparable vertical motions present in cirrus cannot be separated from lidar system frequency fluctuations and measurement noise.

Doppler lidar operation commenced at 1500 on 27 October. The first cirrus clouds were detected to the northwest during VAD scans at about 1900. A prescribed sequence of VAD and RHI scans, and vertical profiles was repeated at one-half hour intervals until  $\sim 0200$  on 28 October, when the cirrus dissipated. Although data collection resumed at 1130, cirrus were not observed until 1230. The data collection sequence continued until the end of operations at 2300, although stratocumulus clouds occasionally disrupted the cirrus observations between 2000 and 2200.

## c. The High Spectral Resolution Lidar

The University of Wisconsin High Spectral Resolution Lidar (HSRL) is a laboratory-based system that was operated from a roof-top facility at the University of Wisconsin-Madison campus. The HSRL technique is distinct from those of the other lidars in that the molecular backscatter component is separable from the cloud backscatter component of the lidar return (Shipley et al. 1983). This is achieved by measuring differences in the spectral distribution of the energy backscattered from the highly monochromatic ( $0.4 \text{ pm}$  bandwidth, FWHM) laser pulse. The rapid thermal motion of the molecules Doppler-



broadens the molecular backscatter spectrum. Aerosols and cloud particles that contribute significantly to the backscatter are considerably more massive, and so are characterized by slower Brownian drift and terminal velocities that produce insignificant spectral broadening. The HSRL observes the return signal in two channels: a spectrally broad channel encompassing the molecular backscatter spectrum, and a spectrally narrow channel centered on the transmitted wavelength, with bandwidths of 2.5 and 0.6 pm, respectively. The two-channel signals are inverted to provide separate profiles of particle and molecular backscattering (Grund and Eloranta 1990). Direct measurement of molecular backscatter allows the calculation of optical extinction, and the ratio of cloud-to-molecular backscatter provides the cloud backscatter coefficient. The normalized backscatter phase function  $P_{\pi}/4\pi$  is determined from the backscatter-to-extinction ratio, since the effects of particle and gaseous absorption at this wavelength are negligible.

Signal detection is accomplished by a pair of photomultiplier tubes operated in a photon counting mode. This detection scheme, coupled with the high pulse repetition rate and low pulse output power of the transmitter (see Table 1), provides the wide dynamic range necessary for cirrus cloud measurements. Because of the narrow beamwidth and narrow spectral bandwidth of the receiver, the effects of multiple scattering and background skylight are suppressed.

A comprehensive analysis of the case study cirrus cloud optical properties, including the assessment of cloud optical thickness  $\tau$ , and a more complete description of the HSRL technique as applied to cirrus measurements may be found in the companion paper by Grund and Eloranta (1990). Vertically-pointing measurements were collected nearly continuously over the case study period, with the exception of occasional system calibration periods.

#### d. The Langley Research Center Fourteen-Inch Lidar System

This versatile system from the Langley Research Center's Aerosol Research Branch was originally designed as an aircraft-based lidar. The current version of the LaRCFILS can be configured in several ways, ranging from a simple, unpolarized system using a single photomultiplier tube to a dual-wavelength, dual-polarization, aircraft-based system using four PMTs. For the Wisconsin FIRE IFO experiment, the ground-based system was configured as a single-wavelength (frequency-doubled Nd:YAG), dual-polarization lidar.

In this configuration, three of the four available PMTs are utilized, with two being multiplexed in order to increase the effective range in the parallel channel, while the third serves as the perpendicular channel detector. The receiver design employs a cube polarizer to separate the two polarization components, and beam splitters in the parallel channel to apportion the collected energy between the dual PMTs in a manner that maximizes channel sensitivity. A unique feature of the receiver design is the incorporation of a half-wave plate mounted on a precision rotating stage. The half-wave plate is used to rotate the polarization plane of the incoming beam for dual-channel calibration purposes in the field when the system measures the linear depolarization ratio. Table 1 presents the pertinent specifications of the system, configured in the manner described above.

Although the lidar unit is coupled to an electrically-driven rotatable

mount for scanning operations, data were collected predominantly in the vertically-pointing mode during the case study. Thin cirrus clouds were first detected at ~1600 on the 27th at this westernmost of the FIRE IFO lidars, and with the exception of a break in the overnight operations from -0200-0800, data were collected nearly continuously until 2359 on the 28th.

#### e. The ER-2 Cloud and Aerosol Lidar System

The ER-2 aircraft is a NASA version of the U-2 high altitude aircraft and is capable of overflying all normally occurring clouds. The Cloud and Aerosol Lidar System (CALS) provides nadir directed elastic backscatter lidar measurements from the ER-2. The system is based on a doubled Nd:YAG laser and includes a dual-polarization receiver. The compact lidar system normally operates at a 5 Hz pulse repetition rate, and at the nominal flight speed of the ER-2 platform, lidar returns are acquired every 40 m along the aircraft flight track. The vertical resolution of the CALS is 7.5 m, but for thin cirrus clouds vertical averaging to larger vertical depths is typically employed. Since the laser power and telescope aperture are relatively modest (Table 1), for some applications such as aerosol profiling or the depolarization of thin clouds, horizontal pulse averaging is also used. A more complete description of the system and operating procedures is given in Spinhirne and Hart (1990).

Since the CALS is operated from a nominal altitude of 19 km, cirrus cloud tops are directly observed. Several kilometers of cloud top cross section can be obtained in a few seconds, and the CALS data essentially freeze an image of the cloud top structure. For sufficiently thin cirrus clouds, lidar signals from the entire cloud and the ground reflection of the laser pulse are received. For more dense clouds, the signal may be attenuated before reaching cloud bottom and the ground return is not seen. The CALS was operated on the ER-2 along with spectral, imaging, and flux radiometers. An interpretation of the passive observations in combination with the ER-2 lidar data is discussed in a companion paper (Spinhirne and Hart 1990).

### 3. Overview of Cirrus Clouds Within the Project Area

#### a. Ground-Based Lidar Observations

A primary motive for dispersing the ground-based lidars over the extended geographical area shown in Fig. 1 was to improve the chances that at least one lidar would be in position to observe cirrus clouds if variable cirrus or obstructing lower-level clouds were present. During the 27-28 October case study, however, cirrus clouds were often distributed throughout the project area, and the ensemble of observations provided a unique image of the spatial and temporal distribution of cirrus clouds over an area of mesoscale proportions. A comparison of the cirrus clouds detected by the four ground-based lidars over the 32-h period is given in the height-versus-time (HTI) displays of Fig. 2. To help interpret the movement of cirrus clouds through the project area, Fig. 3 presents height-time cross sections of middle and upper tropospheric wind and temperature data derived from the special 3-hourly, high vertical resolution rawinsonde observations launched from Fort McCoy.

The combined HTI displays presented in Fig. 2 are gray scale renditions of the log of the range-squared corrected, relative laser backscattering. These images facilitate the qualitative comparison of the data from the significantly

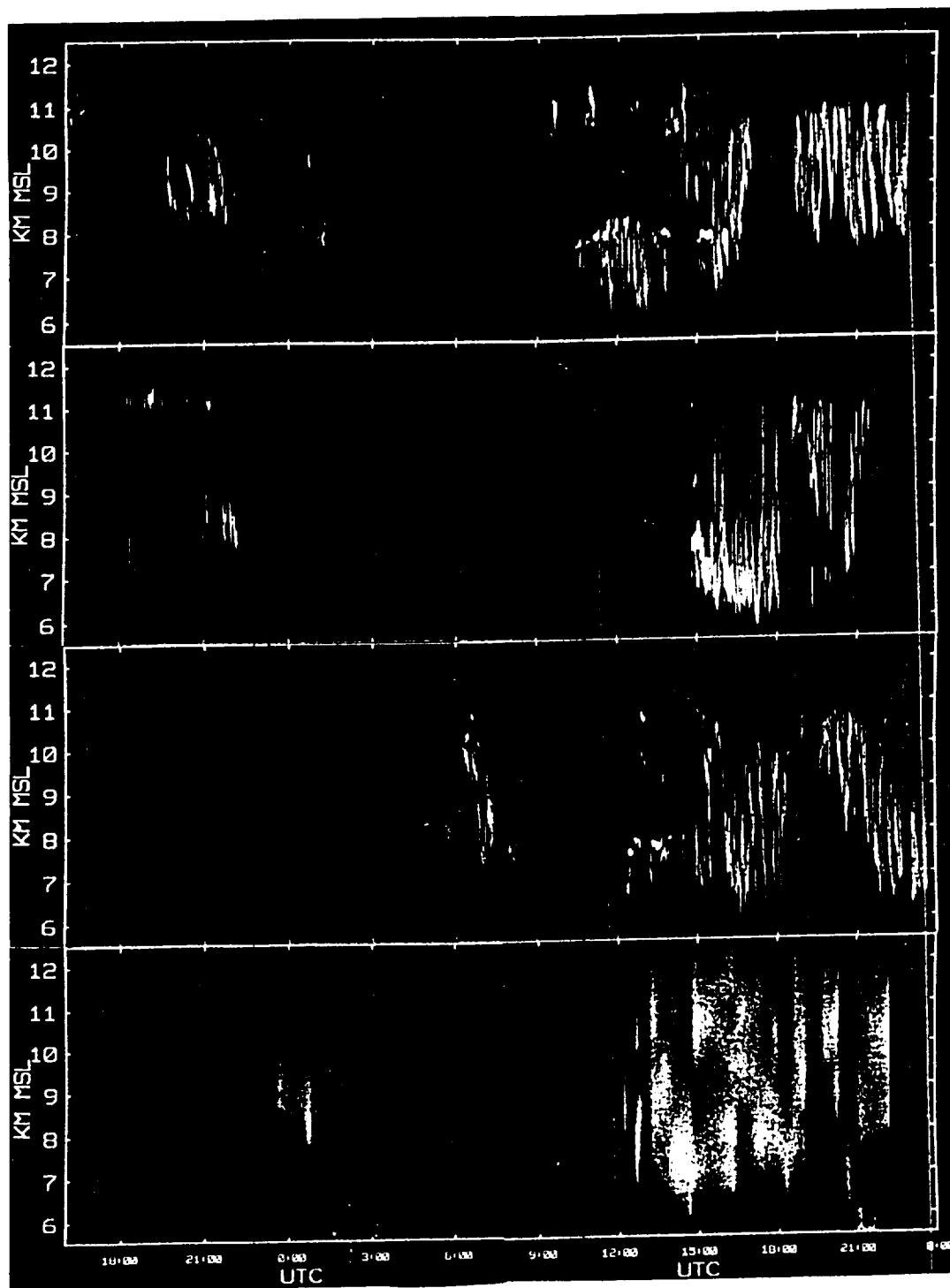


Fig. 2 Combined HTI displays from the four ground-based lidars (from top to bottom, at Fort McCoy, Wausau, Madison, and Oshkosh, Wisconsin) showing clouds detected over a 32-h period. Cloud images are based on a gray scale of the logarithm of relative attenuated laser backscattering, corrected for range-squared effects. Black areas indicate regions where signals fall below useful levels, and the uniformly gray areas delineate missing data periods.

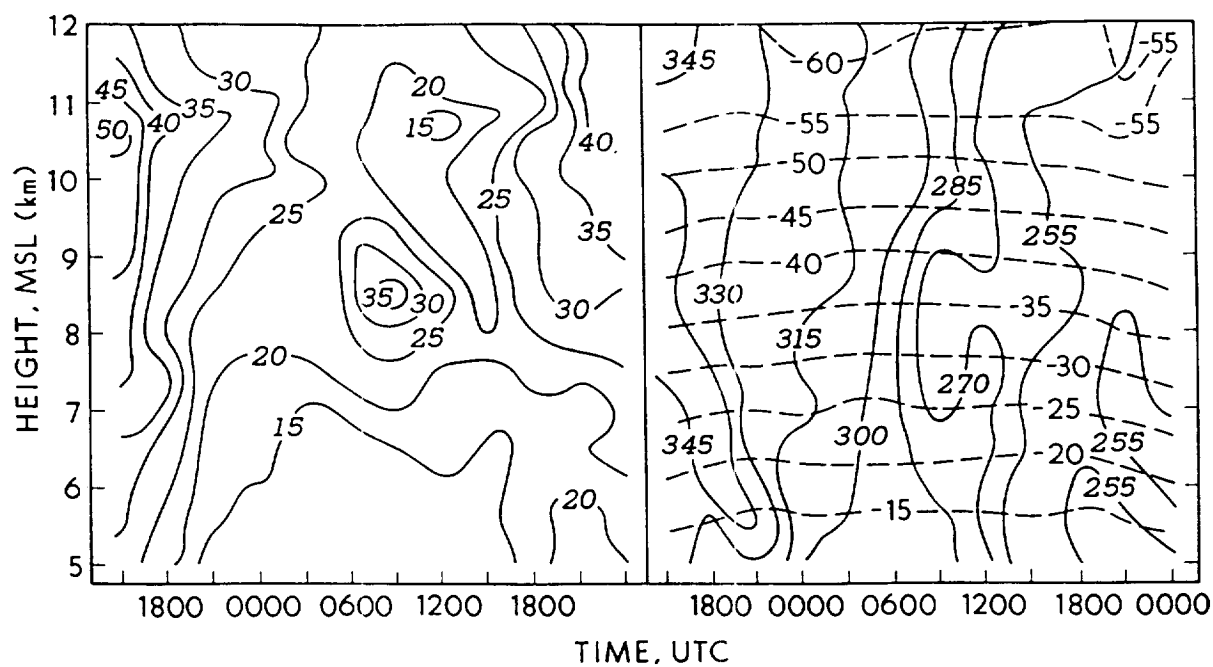


Fig. 3 Time-height cross section of atmospheric wind structure at cirrus cloud altitudes over the case study period. Contours of wind speed (left, in  $\text{m s}^{-1}$ ) and direction (right, in degrees), and temperature (dashed lines, in  $^{\circ}\text{C}$ ) are derived from 3-hourly, high vertical resolution rawinsonde data from Fort McCoy.

different lidar systems. Although somewhat different schemes were employed for the horizontal and vertical averaging of the various datasets, the displays in general preserve much of the spatial and temporal resolutions of each system. With the exception of the Doppler lidar data, only gaps in the data records of  $\leq 10$ -min duration are filled by interpolation. The Oshkosh lidar operations were optimized for the acquisition of wind velocity data from VAD scans, and so vertical profiles were typically obtained at about 30-min intervals. As a result, the WPLDL data in Fig. 2 do not illustrate the true instrument resolution capabilities, and data gaps of  $\leq 1$  h have been filled by linear interpolation. Also note that although the two ground-based polarization lidar systems occasionally scanned off the zenith direction to test for the presence of the anisotropic scattering medium produced by horizontally oriented plate crystals (Platt et al. 1978), only data collected at angles of  $\geq 80^\circ$  are plotted.

Inspection of Fig. 2 reveals that, despite the lapses in coverage from the individual lidars, rather consistent cloud features were observed at the four sites as the cirrus advected through, and developed within, the project area. At the same time, it is clear that a variety of cirrus cloud altitudes and forms, as exemplified in Section 4, were present. According to Fig. 3, average cirrus-level winds gradually backed over the study period from northwesterly to southwesterly, averaging about 25 to 30 m s<sup>-1</sup>, as the crest of the upper level ridge approached and entered the area (see Starr and Wiley 1990). Hence, on average, the cirrus clouds crossed the lidar array along the west-east axis from Fort McCoy to Oshkosh in  $\sim 2$  h, or from top-to-bottom in the sequence given in Fig. 2. However, as will be shown below, the structure present in the high resolution wind data is often connected with the occurrence of the various cirrus clouds. It should be noted that the temperature stratification (dashed lines in Fig. 3) remained rather uniform, reflecting the absence of elevated frontal activity.

The cirrus that occurred over the case study period can be divided into four groups on the basis of synoptic conditions and the appearance of the clouds in ground-based and satellite imagery (see also Starr and Wiley 1990). The four 180° fisheye photographs taken from Wausau in Fig. 4 illustrate the main cloud types. During the first episode, which lasted until  $\sim 0300$  on the morning of 28 October, mesoscale bands of thin (i.e., largely transparent) dissipating cirrus were variably present at primarily two atmospheric levels. The cirrus were more prevalent in the northern sections of the lidar array, just to the south of the dissipating cloud bands observed in satellite imagery (Starr and Wiley 1990). The higher layer typically had a depth of  $< 0.5$  km and a base at 11.0 km. This altitude corresponds to the top of the upper level wind speed maximum shown in Fig. 3, an interface that resembles a weak, secondary tropopause. These clouds were only occasionally visible to the unaided eye in the zenith viewing direction (Fig. 4a). The other cirrus layer, based at  $\sim 8.0$  km, was up to 2.0 km in depth over Fort McCoy and Oshkosh. The all-sky photograph for 2143 (Fig. 4b) shows bands of hooked cirrus fibratus, and the striated cloud structure in the two upper lidar displays in Fig. 2 indicates sheared crystal fallstreaks emanating from generating cells.

The second cirrus cloud episode, although studied only by the Madison lidar between 0500–0800, is a classic example of an isolated mesoscale uncinus complex (MUC), as recently described by Sassen et al. (1989a). This cloud contains a considerable amount of internal structure revealing numerous uncinus cells and fallstreaks. According to satellite imagery, it was a mesoscale cloud band,

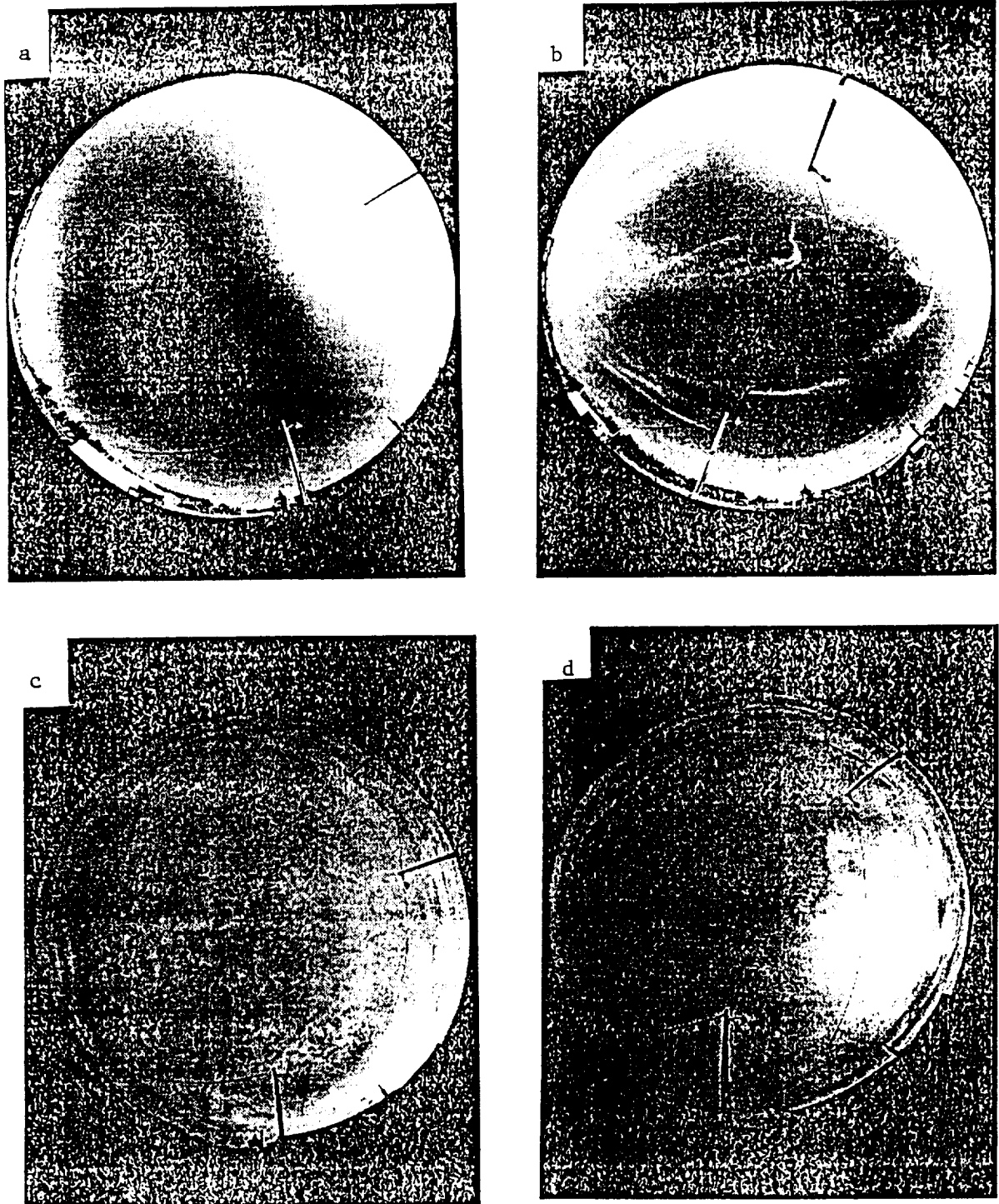


Fig. 4 Four 180° fisheye photographs of clouds over Wausau, taken at (a) 1858 - and (b) 2143 on 27 October, and (c) 1512 and (d) 1711 on 28 October. Cloud movement is approximately from right to left in these images.

oriented in a northwest-southeast direction, that passed directly over Madison (see Grund and Eloranta 1990). The occurrence of this cirrus appears to be linked to the jet wind maximum and directional wind shear features shown at the centers of Fig. 3a and b. The jet core corresponds to the strongest lidar returns measured at ~0720 at the 8.5 km altitude.

Lidar observations after ~1000 on 28 October involve two occurrences of developing cirrus associated with the crest of the approaching longwave ridge. The first of these is particularly interesting in that supercooled altocumulus clouds between about 7.5 and 8.2 km ( $-30^{\circ}$  to  $-35^{\circ}\text{C}$ ) played a role in the development of the up to 5-km thick cirrus from about 1000 to 1830. In terms of atmospheric structure, this altitude corresponds to relatively weak ( $\sim 20 \text{ m s}^{-1}$ ) westerly flow at the exit region of the wind jet (Fig. 3). The cellular appearance of the liquid cloud at the onset of the Wausau observations, just as the altocumulus was becoming embedded within the cirrus, is illustrated in Fig. 4c. Typical water droplet clouds strongly backscatter visible wavelengths, as is indicated by the bright layers intermittently present at ~8.0 km in the three upper displays of Fig. 3. Although ice crystal virga is often present beneath the liquid clouds, water droplet signatures disappear when precipitation from the overlying cirrus or relatively significant amounts of virga are present, indicating frequent cloud glaciation. The particularly (optically) dense cloud over Wausau at times resembled altostratus, although portions of a  $22^{\circ}$  halo were usually observed (Fig. 4d). The ~11.0-km cirrus cloud top height in this case occurs at a wind speed minimum (Fig. 3). The ensemble of middle and upper level clouds corresponds to the wedge-shaped cloud mass observed in satellite imagery to have developed into an organized cloud feature within the lidar array (Starr and Wiley 1990). The sharp boundary with clear air behind the cloud is particularly evident in the Wausau data at 1820.

Cirrus clouds after about 1830 redeveloped primarily from mesoscale complexes of cloud top generating cells at ~11.0 km, from which ice particles precipitated to various depths. Lidar observations often suggest a rather periodic occurrence of more intense generating cell complexes. The visual appearance of these clouds consequently varied from thin, fibrous cirrostratus displaying vivid  $22^{\circ}$  halos, to more dense-appearing cirrus overcasts. Satellite imagery indicates that this patchy cirrus intensified significantly over the project area as cirrus level winds began accelerating in the approaching upper level jet stream.

#### b. Airborne Lidar Observations

Aircraft operations with the NASA ER-2 concentrated on two of the cirrus cloud episodes described above. The 27 October mission (dashed lines in Fig. 1) was conducted in pursuit of the bands of fibrous cirrus from extreme northwestern to west-central Wisconsin. The cirrus clouds probed by the downward-looking lidar during six flight legs are shown in Fig. 5. These height-versus-distance displays consist of gray-scale portrayals of the logarithm of the returned lidar signal. The cirrus clouds detected during this mission were generally between 8.5 and 11.5 km in altitude: a thin but sometimes strongly scattering layer at ~11.0 km, which was observed in northwestern Wisconsin, and a cellular cloud layer typically between 9.0 and 10.0 km. According to Fig. 3, winds within the lower layer at 1900 were northwesterly and displayed a vertical wind shear of  $\sim 4.5 \text{ m s}^{-1} \text{ km}^{-1}$ . The upper cirrus layer at times contains closely-spaced ( $\sim 0.5 \text{ km}$ ) groupings of cells  $< 0.4 \text{ km}$  in depth, which, as shown in

ORIGINAL PAGE IS  
OF POOR QUALITY

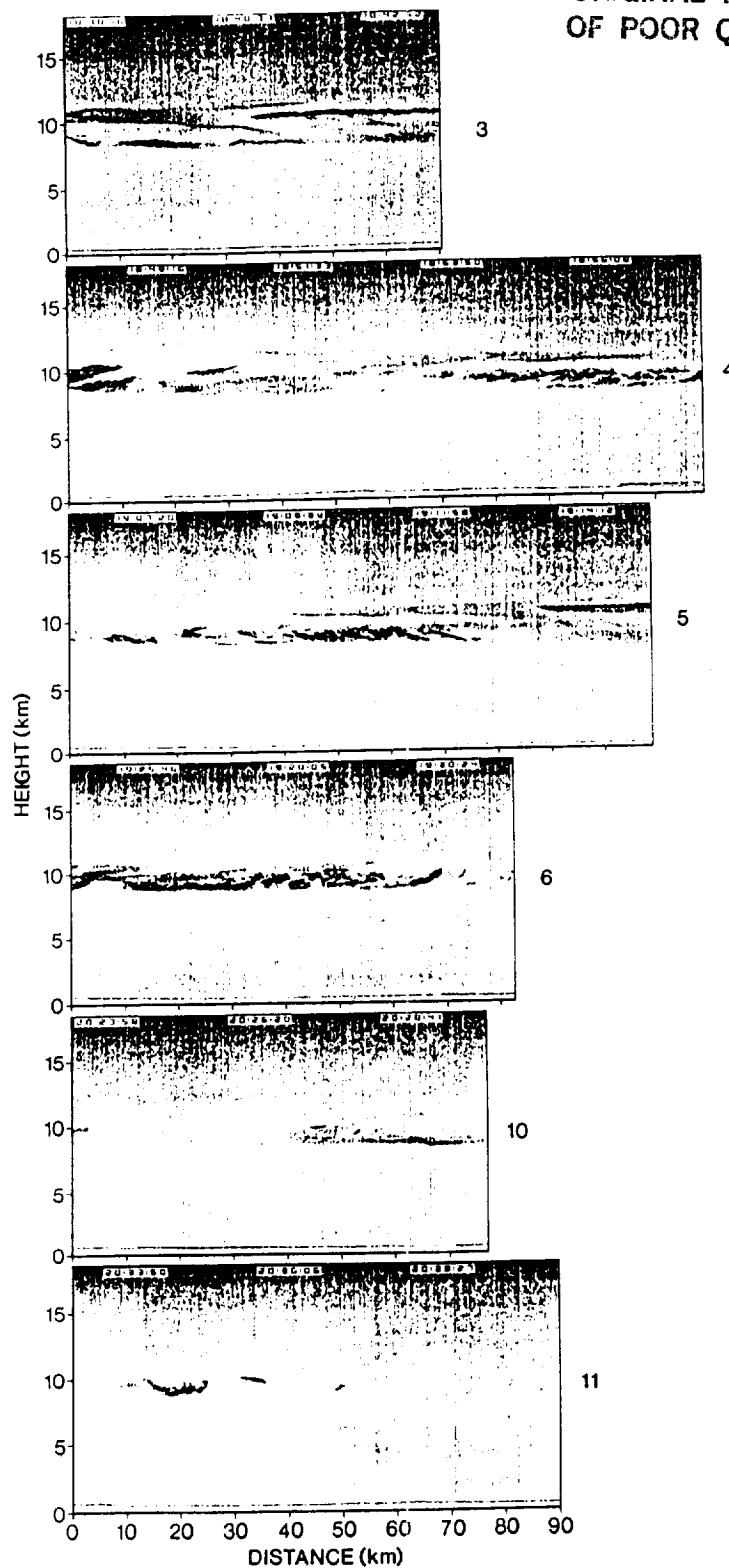
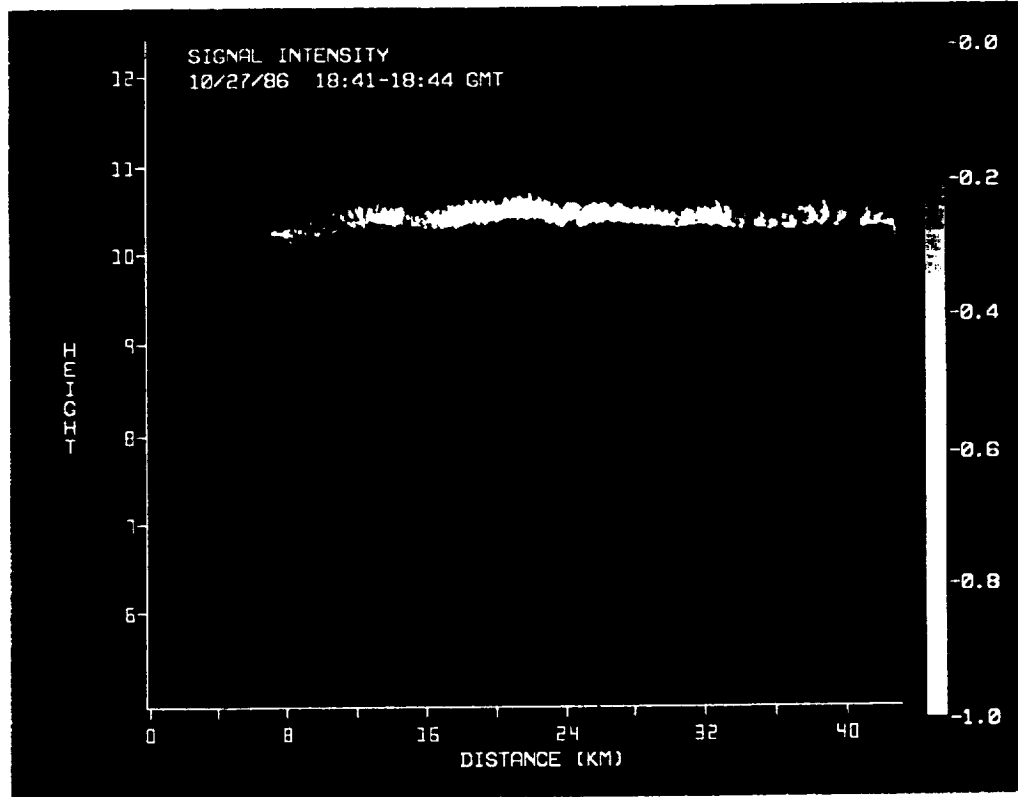


Fig. 5 Range-height displays of cirrus clouds detected by the ER-2 downward-looking lidar during the six flight legs identified at right of each display (see Fig. 1 for geographic locations) on 27 October. The gray-scale darkness of the images is proportional to the logarithm of the received lidar signal.



a)



b)

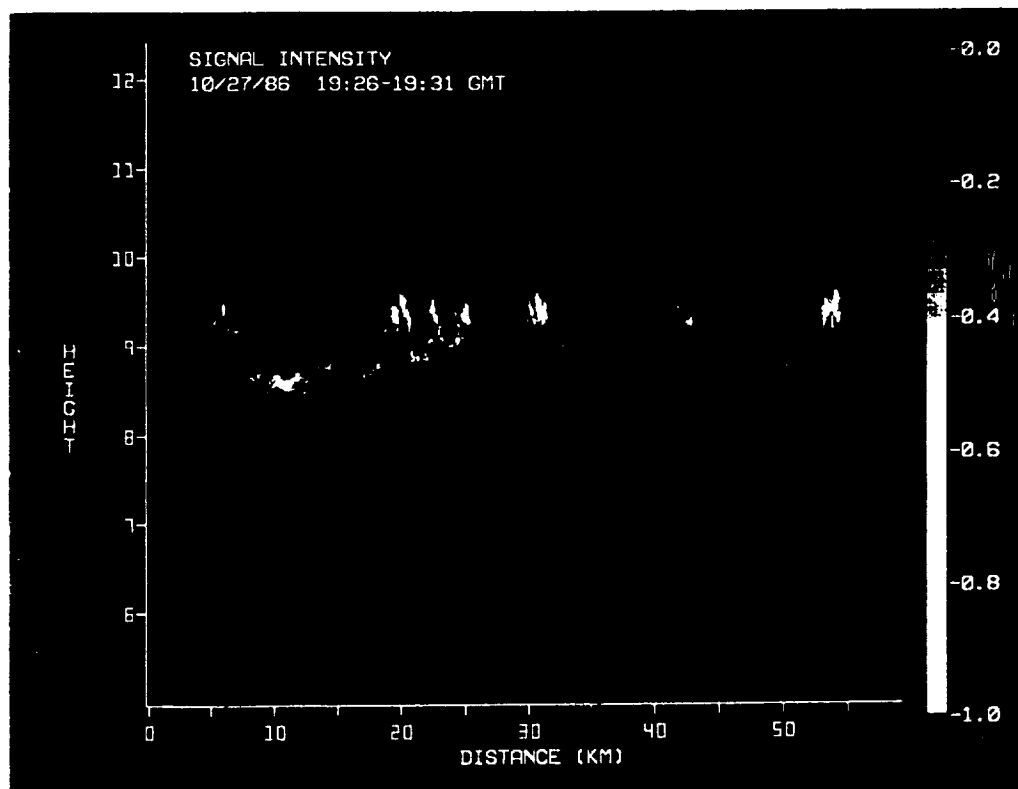


Fig. 6 Expanded views of relative signal intensity from portions of legs 3 (a) and 6 (b), obtained from the downward-looking airborne lidar on 27 October.

the expanded signal intensity display for a portion of leg 3 (Fig. 6a), suggest Kelvin-Helmholtz waves superimposed on a longer wave pattern. More weakly scattering layers with long, vertically sheared fallstreaks were also present. A fine example of the latter feature is depicted at the beginning of leg 3 (Fig. 5), where a ~30-km long precipitation trail exits from a uncinus cell at 10.4 km, indicating a rather low, mean ice particle terminal velocity of  $\sim 0.15 \text{ m s}^{-1}$ .

The structure of the lower cirrus also reflects the sheared environment, often showing clear evidence for sheared crystal fallstreaks emanating from cloud top generating cells at about the  $-40^\circ\text{C}$  level. For example, the slope of the rather linear fallstreak probed at 1912 between 8.75 and 9.50 km altitude during leg 5 (flown approximately along the mean cirrus wind) implies an average ice crystal fallspeed of  $0.45 \text{ m s}^{-1}$ , which is consistent with the terminal velocity of bullet rosette crystals of 0.22 mm diameter (Heymsfield 1975). The strongly scattering uncinus cell heads noted during leg 6 are 1-2 km across, and sprout curved fallstreaks that appear to define the cloud base at 9.0 km (see Fig. 6). Data collected within the central part of the lidar array (legs 10 and 11) show only variable, weakly scattering cirrus clouds between 8.5 and 10.0 km.

Flight operations on 28 October were conducted in close coordination with the ground-based lidar stations (Fig. 1, solid lines). Primarily, the wedge-shaped mass of dense cirrus was probed between ~8.0 and 11.0 km altitude as this feature was exiting the lidar array. The well-defined rear edge of this cirrus is apparent in the data for leg 6 (Fig. 7) as the ER-2 approached Fort McCoy from Wausau, and then again east of Fort McCoy during leg 7, and appears to have caused strong attenuation. Comparison with satellite imagery indicates that the irregular southern tip of this cirrus was sampled around Madison (legs 8 and 9), but that a portion of the more organized cloud was again overflown from ~70 to 130 km north of Madison during leg 9. The two relatively short (~100 km), identical flight segments of legs 2 and 4 were collected approximately into the mean cirrus wind, to the west of Wausau. Leg 4 extended nearly to the position then occupied by the edge of the cirrus. Note that since these two legs are separated by 22.4 min, the displacement of the irregular but strongly scattering cloud layer from 8.0 to 9.0 km by ~30.0 km is in compliance with the  $20 \text{ m s}^{-1}$  advection velocity and implies some longevity and areal distribution to these clouds, despite changes in the fallstreak patterns aloft.

Detailed examination of these six flight legs reveals that thin but strongly scattering cloud layers were occasionally observed at altitudes of about 11.0, 8.0, and 4.0 km. The upper layer was incorporated into the denser cirrus near the trailing edge of the cloud mass, but at other times remained narrowly separated. As shown in the expanded signal intensity display for leg 6 (Fig. 8), small (<1.0 km) isolated uncinus cells were observed at this level from 50 to 75 km distance, and at ~40 km, a "z" shaped cloud centered around the 10.8 km altitude wind speed minimum (Fig. 3) occurred in response to the wind shear. The layer at ~8.0 km corresponds to the altocumulus described previously. This layer is sometimes associated with more diffuse-appearing virga (legs 2, 4, and 8), and tends to display a cellular appearance, particularly at 1734 (leg 7). The lowest layer corresponds to the stratocumulus clouds that were observed in the Fort McCoy region around 1720.

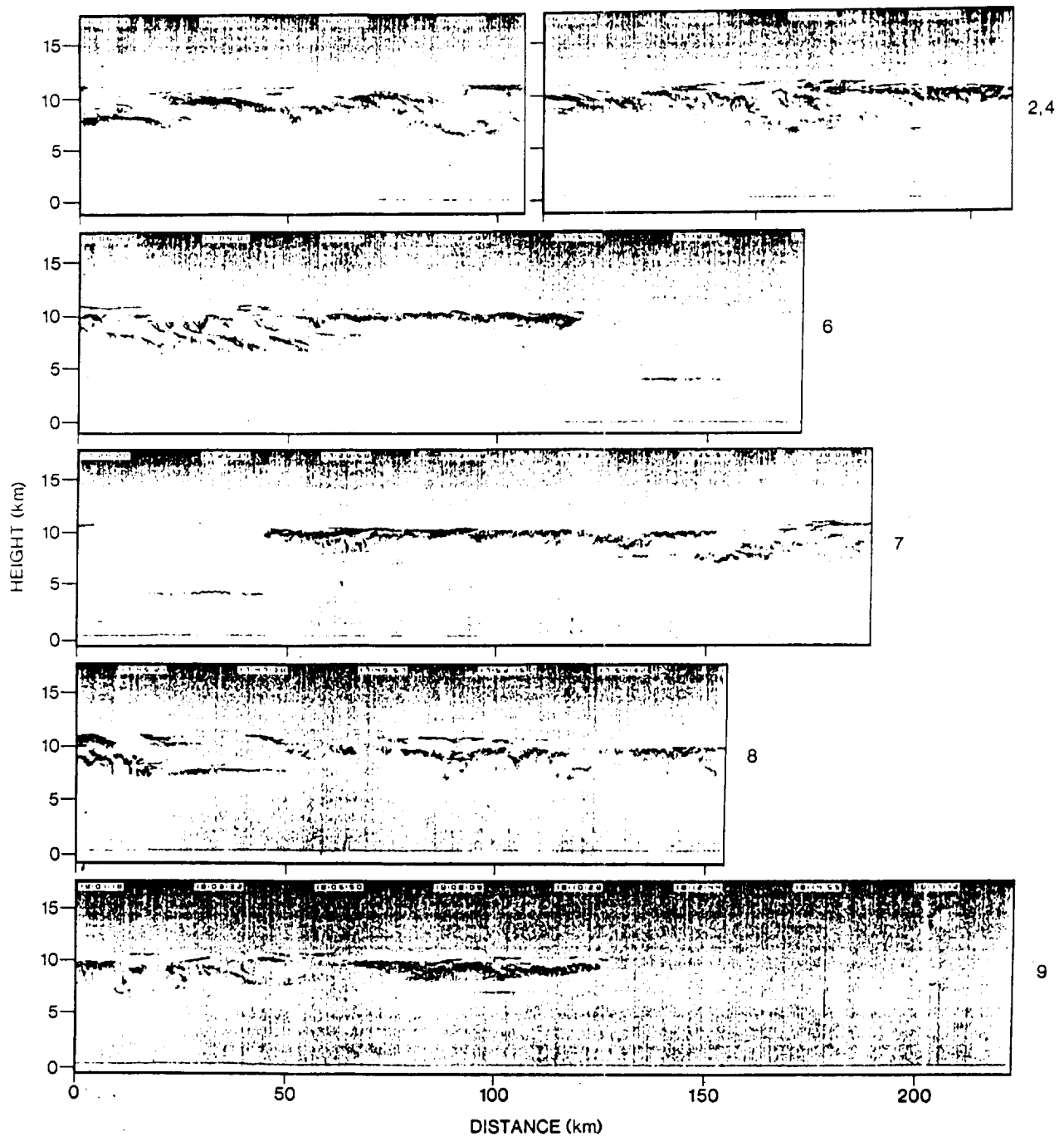
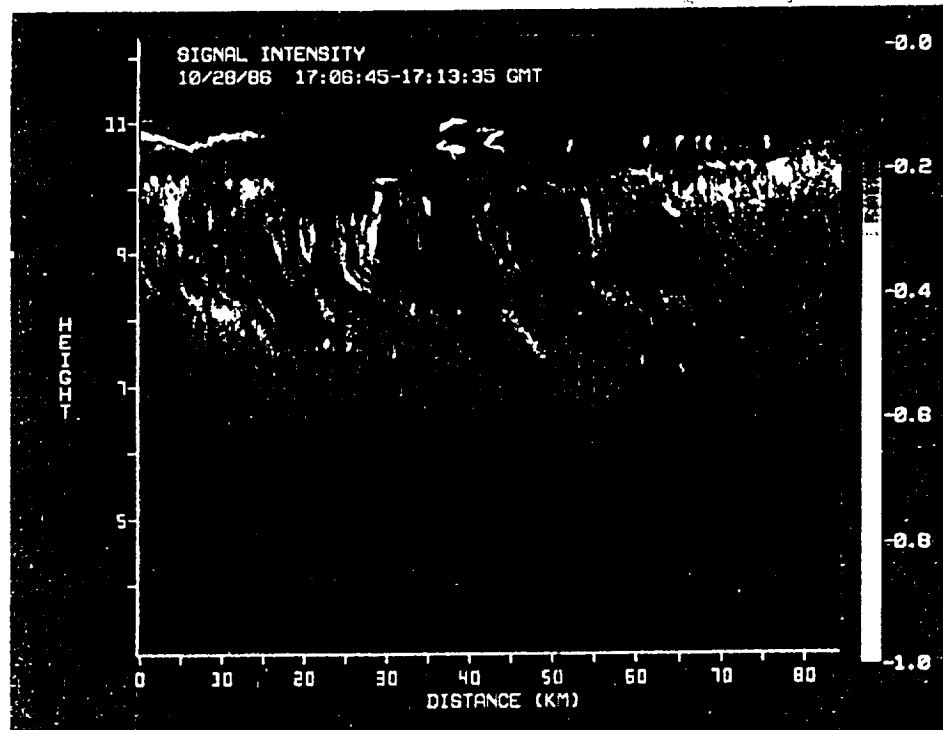


Fig. 7 Range-height lidar displays obtained by the ER-2 platform, as in Fig. 5, but for six flight legs on 28 October.

a)



b)

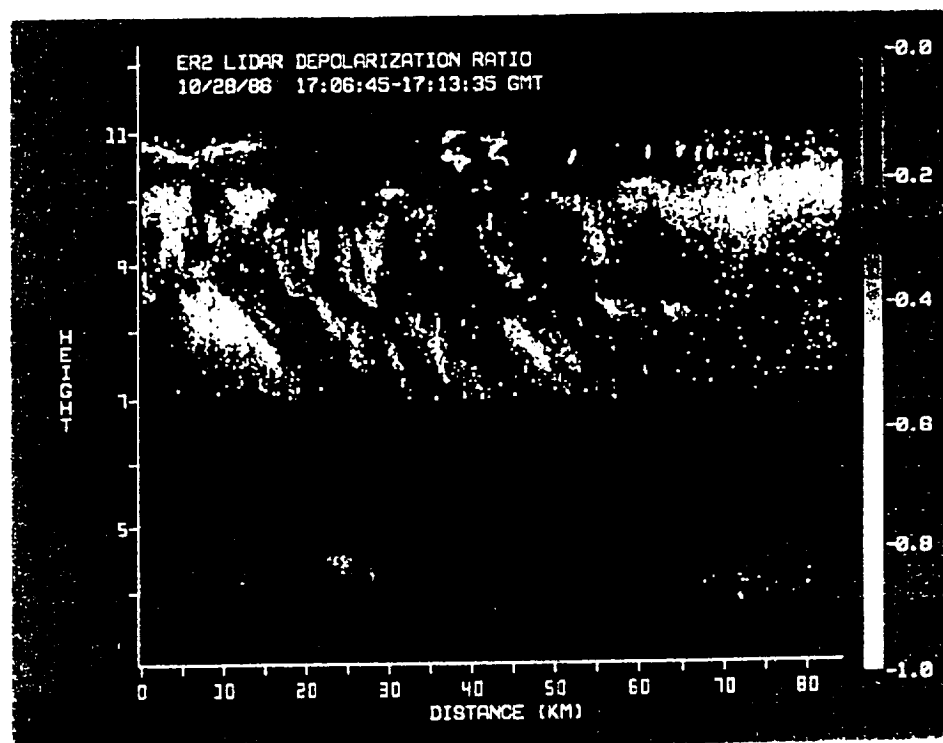


Fig. 8 Expanded view of ER-2 lidar data in terms of (a) relative signal intensity and (b) linear depolarization ratio for a portion of leg 6 on 28 October. The 1707:20 overpass of the Wausau lidar occurred at 12.0 km on the distance scale.

#### 4. Cirrus Cloud Observational Highlights

The previous remote sensing data overviews have placed the cirrus clouds in the context of the synoptic setting, and pointed out some basic features of the various clouds, which are explored in greater detail in this section by exploiting additional measurement capabilities of the lidars. These descriptions are broken into the four cirrus cloud episodes delineated in Section 3a.

##### a. Subvisual and Thin Cirrus: 1600 (27 October) - 0300 (28 October)

Analysis of these tenuous clouds provides reliable information on cloud optical thickness  $\tau$  and linear depolarization properties. In Fig. 9 are given HTI displays of  $\delta$  and estimated  $\beta_{\pi}$ , and a trace of  $\tau$  values derived from the Wausau lidar data for the upper and lower cirrus layers. The analysis procedures are the same as those recently described by Sassen et al. (1989b), in which the  $\delta$  values are adjusted for molecular scattering. A value of  $k = 0.028 \text{ sr}^{-1}$  was calculated for the backscatter-to-extinction ratio based on the  $P_{\pi}/4\pi$  values collected at ~2300 by the HSRL (Grund and Eloranta 1990), and a multiple scattering correction factor  $\eta = 0.5$  was employed in recognition of the 3.0 m receiver beamwidth and assuming the presence of relatively large ice particles. The findings from the mostly zenith subvisual cirrus clouds are quite similar to those reported by Sassen et al. (1989b) for a different FIRE IFO case study, showing a threshold  $\tau$  for visual detection in the zenith direction (compare Figs. 4a and 9) of ~0.03, and  $\delta$  values of ~0.4. The upwind cirrus clouds at these altitudes, according to the airborne lidar (Fig. 6a), were sometimes associated with shallow generating cells.

The lower cirrus, which is clearly composed of complexes of generating cells and fallstreaks, often yielded considerably higher  $\tau$  values, but lower  $\delta$  values, according to the Wausau lidar display of Fig. 9. In keeping with the maximum  $\tau$  of 0.1-0.4, the particle fallstreaks were easily visible as they passed overhead (Fig. 4b). As observed in a similar, but more developed group of mesoscale cloud bands (Sassen et al. 1989a), uncharacteristically low  $\delta$  values ( $< 0.2$ ) seem to be associated with generating regions both in the advanced isolated cells and the main cloud band. In the remainder of the cirrus,  $\delta = 0.25-0.35$  are usually present, which may reflect ice crystal evaporation effects in the largely dissipating cloud (Starr and Wiley 1990). The diffuse cloud boundaries and lack of well-organized cloud top generating structures also implies cloud dissipation. Recall that airborne lidar probing to the west of Wausau at ~1930 (Fig. 6b) identified more vigorous generating cells, which contained mostly  $\delta = 0.4-0.5$ .

Scanning Doppler lidar observations show that very scattered cirrus clouds at both atmospheric levels continued to move through the Oshkosh area until ~0130 on the 28th. The clouds were more prevalent to the north and northwest of the site. Derived 10.6  $\mu\text{m}$  cloud optical thicknesses (Hall et al. 1988) were typically  $\ll 0.1$ , with backscatter coefficients on the order of  $10^{-6} (\text{km sr})^{-1}$ . (Note that, due primarily to the strong absorption by ice and water at the 10.6  $\mu\text{m}$  wavelength, and perhaps to size parameter scattering effects, the  $\text{CO}_2$  lidar  $\beta_{\pi}$  are considerably smaller than their visible wavelength counterparts.) However, observations at 0045 probed a ~2-km thick cirrus with a base at ~7.5 km, which produced peak  $\beta_{\pi}$  of  $\sim 7 \times 10^{-5} (\text{km sr})^{-1}$ . This cloud yielded  $\tau$  of 0.1 to 0.2, but the cirrus soon thinned appreciably.

ORIGINAL PAGE IS  
OF POOR QUALITY

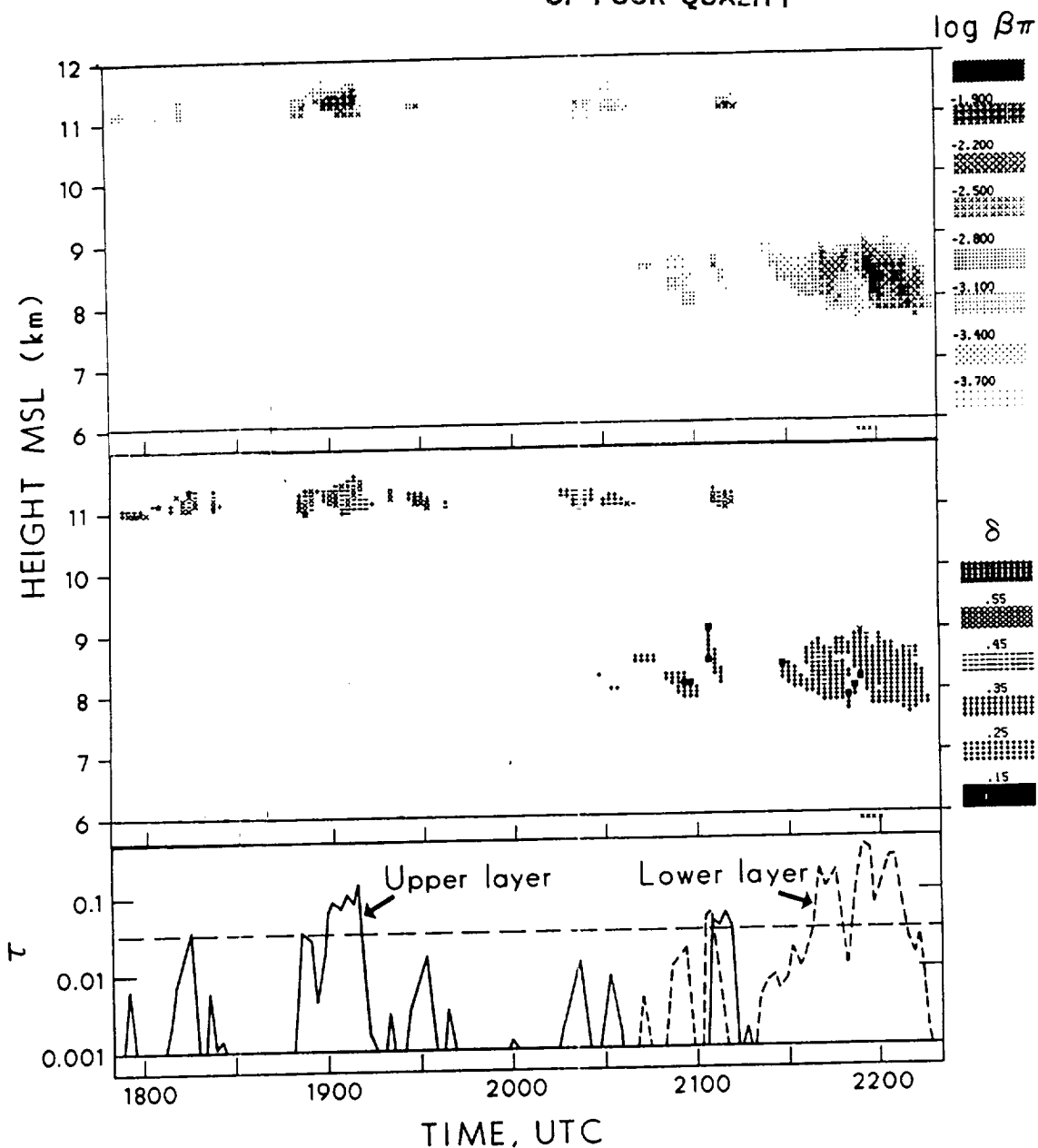


Fig. 9 HTI displays of (a) estimated volume backscatter coefficient in logarithmic units of  $(\text{km sr})^{-1}$  and (b) linear depolarization ratio  $\delta$  (see keys), and cloud optical thickness  $\tau$  values (with log scale) for Wausau lidar observations of subvisual and fibrous cirrus clouds probed on 27 October. Dashed line at  $\tau = 0.03$  represents the approximate threshold for visual cloud detection.

b. The Isolated Mesoscale Uncinus Complex: 0500-0800 (28 October)

As mentioned above, only the Madison HSRL system was operational overnight to study this interesting mesoscale cloud formation. An expanded gray-scale HTI display of the 0500-0900 period for this lidar is presented in Fig. 10a. Several important features are evident in this high temporal resolution image. The period around 0700 shows a striated structure characteristic of fallstreaks that occur at a ~3-4-min periodicity, implying a separation of generating cells of ~5 km. The uncinus cells generating the fallstreaks appear to have dimensions on the order of ~1-2 km. In addition, there seems to be a repeated pattern of enhanced backscatter at a ~20-min time scale. These are most notable at 0620 and 0640 near 10 km, where the cloud top structure is suggestive of vigorous convective activity. The overall appearance of this organized cloud structure clearly fits the description of a mesoscale uncinus complex (MUC). Based on an estimate of  $25 \text{ m s}^{-1}$  for the mean wind, the structure between 0620 and 0740 is estimated to be ~120 km across, assuming that the temporal evolution of the cloud was relatively unimportant as the band drifted over Madison.

Figure 10b provides the corresponding display of volume backscattering coefficients produced from the inverted, time-averaged (~12 min) cloud particle-to-molecular backscatter ratio. The steep contour gradient at 0700 at 7.2 km altitude is an indication of rapid ice crystal evaporation in a dry subcloud environment. The concentration of contours centered at 8.5 km around 0720 appears to result from cirrus cloud growth processes triggered by the sedimentation of ice crystals into the then dry subcloud environment, as previously indicated by both theoretical (Starr and Cox 1985) and experimental (Sassen et al. 1989a) findings. In this case the cloud formation processes are associated with a jet wind maximum at 8.5 km (see Fig. 3). HSRL data averaged over the 0600-0750 period indicate a mean optical thickness of  $0.58 \pm 0.05$ .

c. The Cirrus/Alto cumulus Cloud Mass: 1000-1830 (28 October)

The essentially Eulerian view provided by the downward-looking airborne lidar is particularly useful in this case for establishing the dominant cirrus generating mechanism. (The ground-based lidars were often prohibited from obtaining consistent images of the important middle and upper portions of the cloud due to strong attenuation in the lower cloud.) As is particularly evident from the expanded display of aircraft leg 6 data (Fig. 8), the source of the ice particles at cloud base can typically be linked to sheared particle fallstreaks emanating from generating regions between 9.5 and 10.0 km. The slopes of the fallstreaks in the layer from about 7.0 to 8.5 km, which displayed an average vertical wind shear of  $\sim 5 \text{ m s}^{-1} \text{ km}^{-1}$ , imply the presence of ice particles with  $\sim 1.0 \text{ m s}^{-1}$  average terminal velocities. These strongly scattering particles were likely ice crystal aggregates, as were observed by the King Air aircraft in the vicinity of Wausau at this time (see Heymsfield et al. 1990). The fallstreak from 5 to 20 km distance shown in the ER-2 data of Fig. 8 was in the process of descending over Wausau (see also Kinne et al. 1990). According to the Wausau lidar data, this fallstreak reached cloud base at ~1720, producing virga that protruded ~0.5 km below the usual cloud base altitude (see Fig. 11). The fisheye photograph for 1711 (Fig. 4d) shows the fallstreak as a darker cloud feature, which is beginning to obscure the 22° halo, advancing over the Wausau site.

Figure 11 also shows that the image of the cirrus cloud base region pro-

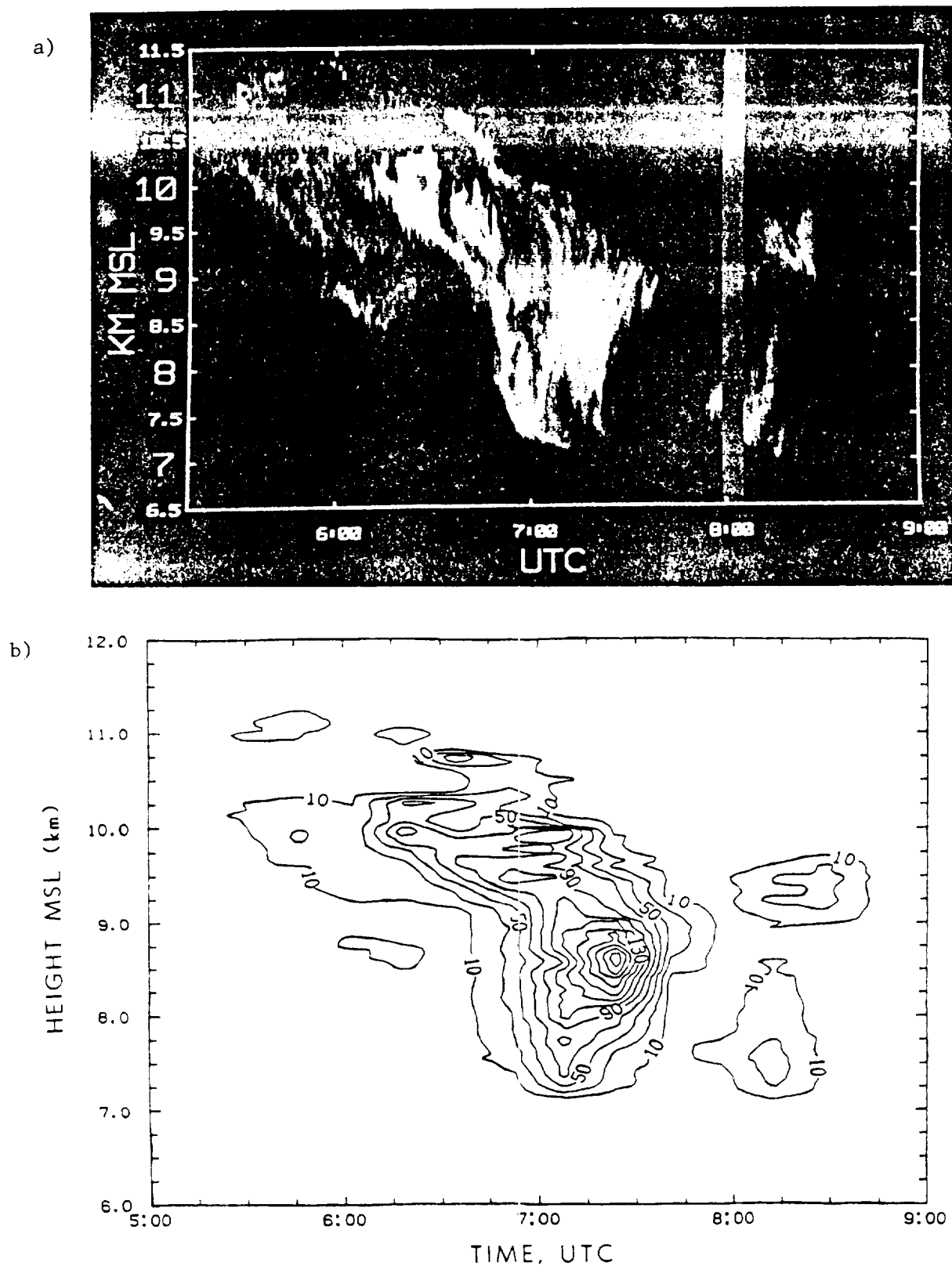


Fig. 10 Expanded HTI displays of the MUC observed by the Madison HSRL system early on 28 October, in terms of (a) a gray-scale plot of relative laser backscattering (as in Fig. 2) and (b) derived backscatter coefficients in units of times  $10^{-4} \text{ (km sr)}^{-1}$ .



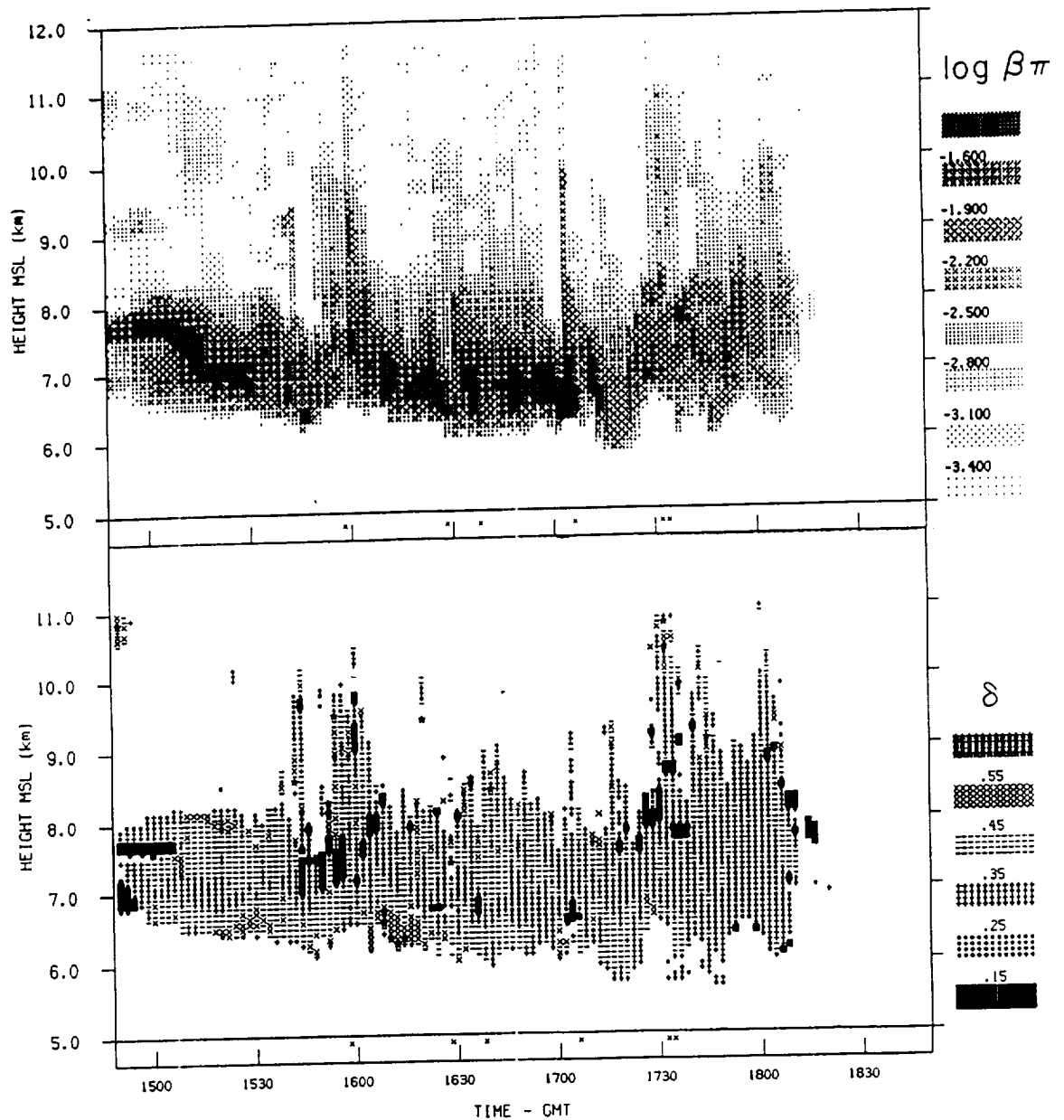


Fig. 11 Estimated volume backscatter coefficients in logarithmic units of  $(\text{km sr})^{-1}$  and  $\delta$  values (note keys) derived from Wausau lidar measurements, showing sporadic liquid phase altocumulus clouds embedded within the lower cirrus at about 6.8 and 3.0 km. Attenuation often appears to have limited the depth of lidar probing.

vided by the Wausau MPL lidar data is, in contrast to the airborne observations, considerably more continuous. Obviously, nadir-directed lidar attenuation often prohibited observing the cloud base particles present between the denser particle fallstreaks. The explanation for the presence of the lower cirrus in the absence of the fallstreaks, as mentioned previously, is related to the intermittent detection of supercooled ( $\sim -30^\circ$  to  $-35^\circ\text{C}$ ) altocumulus clouds, which produced both virga and glaciated ice crystal layers. (Note the small, strongly scattering altocumulus cloud present at a height of 7.7 km and a distance of 23 km in Fig. 8a occupying a position between two particle fallstreaks.) Although the evidence for supercooled liquid clouds provided thus far has been based on the strong laser backscattering properties of thin cloud layers, this ambiguous signature is confirmed by the airborne and ground-based laser depolarization data given in Figs. 8b and 11-13.

Lidar backscattering and polarization data, which reveal the low ( $\delta < 0.15$ ) depolarization ratios consistent with cloud droplet scattering, are given in Figs. 11 and 12 for the Wausau and Fort McCoy lidars, and in Fig. 13 for a segment of leg 8 from the airborne lidar. At the beginning of the period shown in Fig. 11, a supercooled liquid altocumulus cloud (Fig. 4c) at 7.6 km is only briefly detected prior to becoming glaciated by the thickening cirrus. However, sporadic evidence for altocumulus between 7.5 and 8.0 km is indicated by low depolarization and strong backscattering, particularly when only comparatively weak ice crystal scattering is present. Also note from Fig. 11 that thin liquid layers were occasionally detected at  $\sim 6.8$  km within the lower cirrus cloud (e.g., at 1445, 1630, and 1710). As shown in the fisheye photograph for 1711 (Fig. 4d), these layers were patchy altocumulus clouds that visually appeared bright and displayed solar iridescence effects.

The data record from Fort McCoy (Fig. 12) provides an obvious water cloud signature, with associated virga, from 1500 to 1535. After this time, ice particles precipitating from the cirrus aloft temporarily glaciated the liquid cloud. Interestingly, there is depolarization evidence that the riming process contributed to the dissipation of the liquid layer. That is, the  $\delta$  values along the leading edge of the fallstreak increase from  $\sim 0.4$  to up to 0.65 from above to below the former liquid cloud base, a pattern quite similar to that observed during lidar and aircraft studies of ice particle riming in orographic clouds (Sassen 1978). The occasional presence of relatively strong backscattering and low  $\delta$  values after the initial cloud glaciation shows the reemergence of liquid or mixed-phase clouds at  $\sim 8.0$  km in the absence of strong cirrus particle precipitation. The liquid-phase stratocumulus clouds observed at 4.2 km beginning at  $\sim 1700$  also display quite low  $\delta$  values.

The airborne lidar display of Fig. 13 also clearly illustrates the distinction between typical droplet and ice crystal cloud backscatter depolarization behaviors. Ice cloud  $\delta$  values average  $\sim 0.5$ , in contrast to the  $< 0.15$  values present in the thin, cellular altocumulus layer at 7.8 km. Note that the occurrence of similarly low  $\delta$  values in thin layers near the cirrus cloud top can most likely be explained by the specular reflections from oriented plate crystals, analogous to previously documented zenith-pointing lidar effects (Platt et al. 1978). The  $\delta$  value display in Fig. 8b similarly confirms the presence of the liquid-dominated cloud element at 7.6 km altitude between two particle fallstreaks displaying  $\delta \approx 0.55$  values.

Although of a more indirect nature, the HSRL normalized backscatter phase

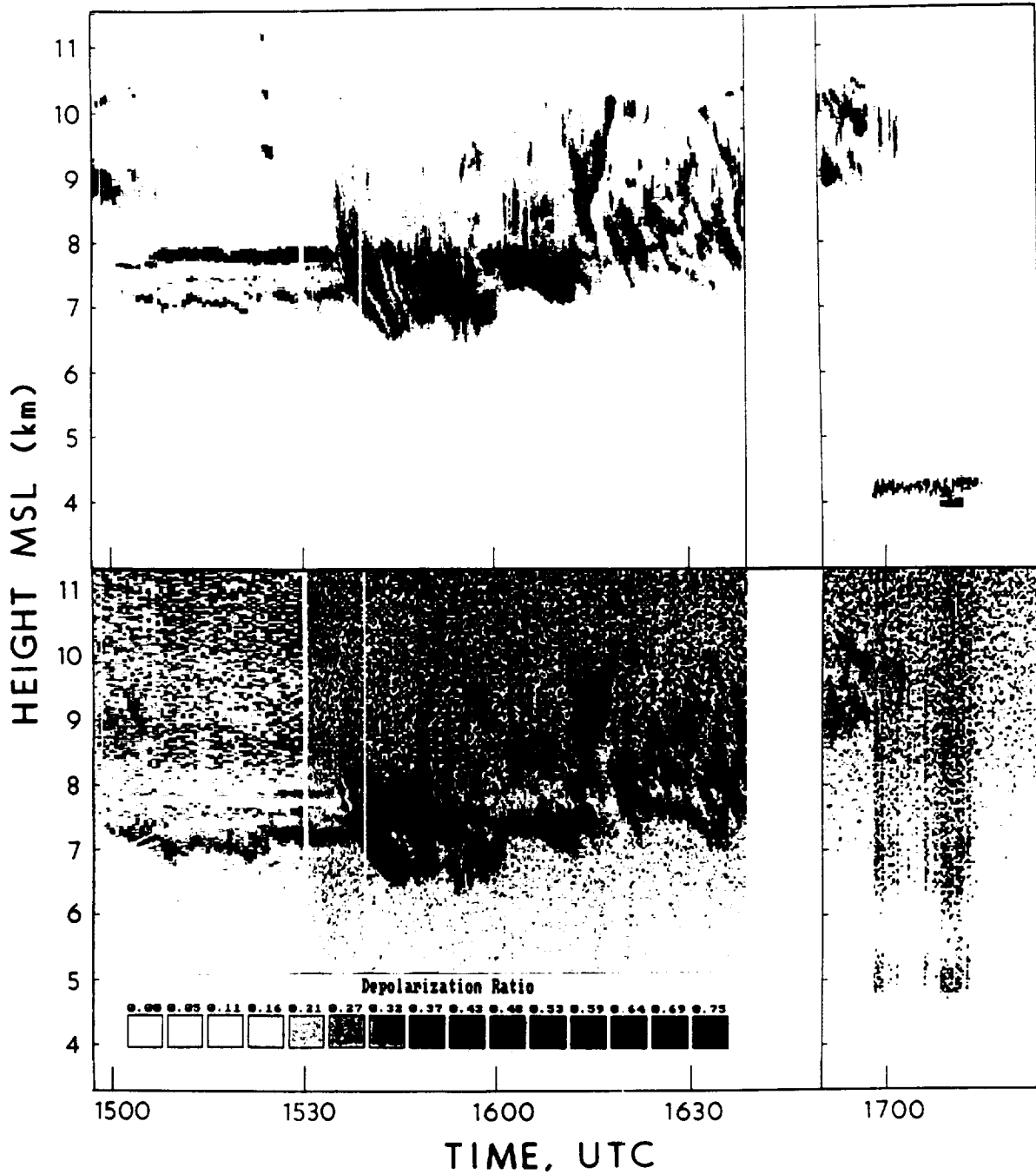


Fig. 12 Expanded gray-scale displays of (a) relative laser backscattering in logarithmic units and (b)  $\delta$  values from the Fort McCoy lidar, showing virga production from, and the glaciation of, supercooled altocumulus clouds at  $\sim 7.8$  km. Note the effects of signal noise in weak, attenuated signals as the dark areas in the  $\delta$  display.

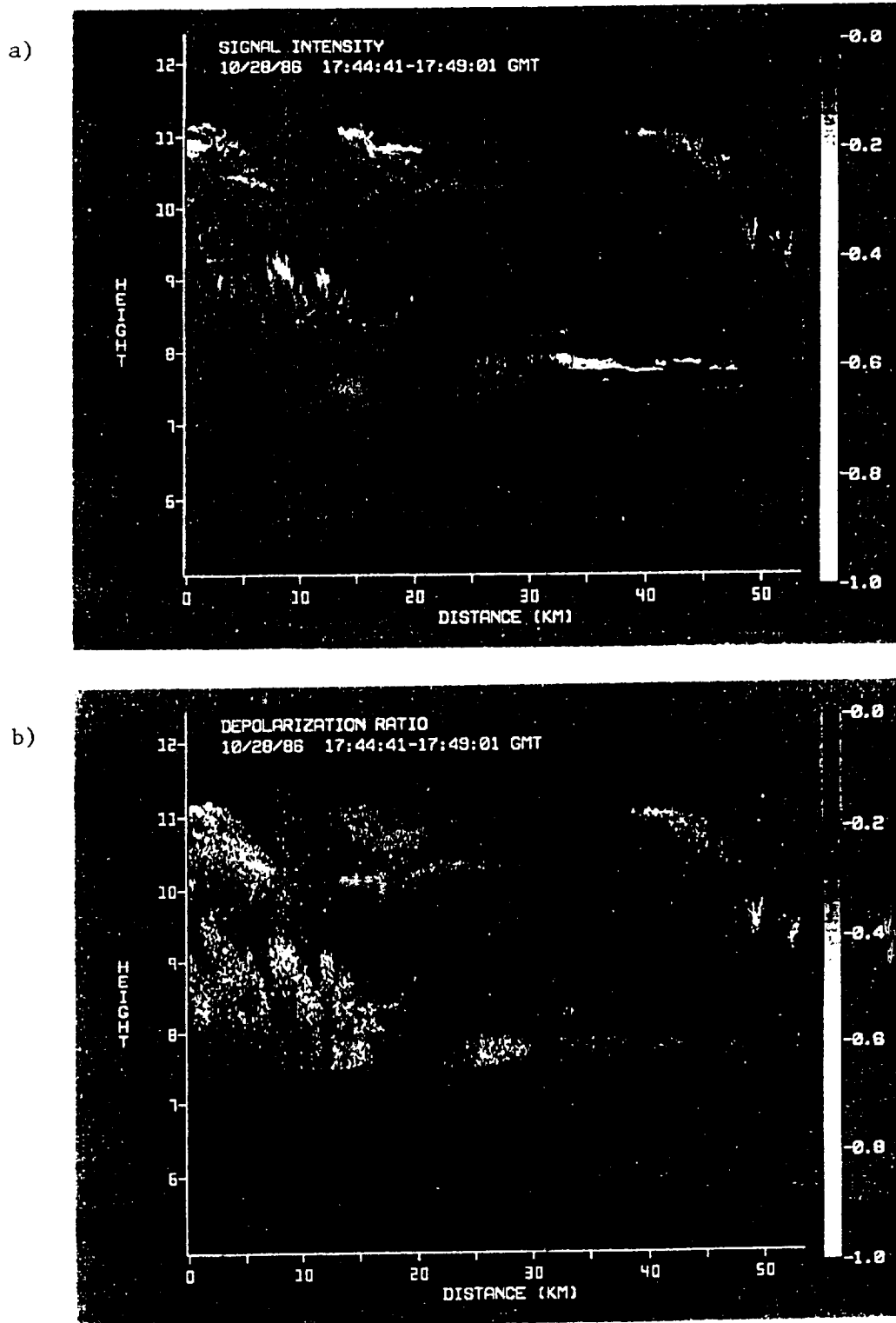


Fig. 13 Expanded (a) relative returned laser signal and (b)  $\delta$  value displays from a portion of leg 8 obtained by the ER-2 lidar on 28 October, revealing liquid-phase altocumulus clouds at  $\sim 8.0$  km.

function  $P_{\pi}/4\pi$  values given in Table 2 for the strongly scattering (note peak  $\beta_{\pi}$  values) clouds at  $\sim 8.0$  km (Fig. 14) are quite different from those for the surrounding ice clouds. Based on the agreement of the  $P_{\pi}/4\pi$  values for typical cloud droplet spectra given in Platt and Bartusek (1974), this analysis also provides strong, but not unambiguous, evidence for the presence of supercooled altocumulus clouds over Madison.

The scanning and zenith data collected by the Doppler lidar at Oshkosh also indicate the presence of cloud-base altocumulus, deep striated cirrus, and the thin capping cirrus layer, even though these features may not be apparent in the HTI display of Fig. 2. A cloud layer was first observed at 1210 extending from 7.2 to 8.7 km, which is consistent with the altocumulus and virga noted at times from the other sites. Peak average  $\beta_{\pi}$  were only  $6 \times 10^{-6}$  (km sr) $^{-1}$ , however, probably indicating that the supercooled cloud droplets were mostly small in comparison to the  $10.6 \mu\text{m}$  wavelength. Over the ensuing 2.5-h period the cirrus cloud system gradually developed in vertical thickness and backscattering coefficients increased, yielding maximum  $\beta_{\pi} \approx 10^{-4}$  (km sr) $^{-1}$ . As the cirrus dissipated somewhat over Oshkosh from  $\sim 1500$  to 1700, a higher cloud base and a layered structure were observed. The 6-min HTI display for 1525 in Fig. 15, for example, shows three cloud layers between  $\sim 7.0$  and 11.5 km. The middle layer at  $\sim 8.0$  km is intermittent and may represent scattered altocumulus clouds, from which virga appears to trail to define the lower cloud base. The PPI scan for 1609 (Fig. 16) also shows the presence of three or four intermittent layers ranging from 7.7 to 10.3 km altitude. (Note that the inner ring of signals represents aerosol scattering from within the boundary layer.) The boundary layer and cirrus cloud level winds computed from this VAD scan sequence are given in Fig. 17. Comparison with Fig. 3 indicates reasonable agreement with concurrent rawinsonde data at cirrus cloud altitudes, although the Doppler-derived wind speeds over Oshkosh tend to be  $\sim 10 \text{ m s}^{-1}$  greater than those from the Fort McCoy soundings.

#### d. Developing Mesoscale Cirrus: 1830-2359 (28 October)

Data collected during this final period are best illustrated by the Fort McCoy lidar dataset (Fig. 18). In general, following the passage of the dense cirrus cloud mass depicted in satellite imagery, deep cirrus clouds were observed to periodically redevelop from mesoscale cloud top generating regions at 11.0 km. From  $\sim 1835$  to 2215, a fairly regular appearance at  $\sim 50$ -min intervals (roughly 90 km distances in the accelerating upper level jet) of cirrus generating regions is apparent. These developments are associated with periodic enhancements in the strengths of the cloud top generating cell complexes, and give the cirrus a serrated appearance due to the variable virga penetration depths. Over Fort McCoy after  $\sim 2230$ , however, a more continuous progression of cloud top generating cells is apparent in Fig. 19a, along with a gradually decreasing cloud base altitude. The  $\delta$  value display of Fig. 19b indicates that the generating cell/fallstreak features are also often linked to linear depolarization patterns that can be followed through the cloud, indicating a maintenance of ice crystal shape (i.e., aspect ratio) during descent.

From Fig. 2, a similar development of cirrus from cloud top generating regions is apparent over Madison, although ice crystal precipitation is more vigorous, with the cirrus cloud base approaching 6 km. Over Wausau, only a single, but larger-scale descending cirrus cloud mass was observed through the increasing interference caused by stratocumulus clouds based at 3.9 km.

Table 2 HSRL normalized backscatter phase function  $P_{\pi}/4\pi$  and additional data for the altocumulus and surrounding ice clouds on 28 October.

| Time<br>(UTC) | Altitude<br>(km, MSL) | $P_{\pi}/4\pi$<br>( $\text{sr}^{-1}$ ) | Peak $\delta_{\pi 1}$<br>( $\text{km sr}^{-1}$ ) | $\tau$            | Analysis               |
|---------------|-----------------------|--|--|-------------------|------------------------|
| 1150-1228     | 10.0-12.1             | $0.020 \pm 0.012$                      | 0.001  | $0.023 \pm 0.011$ | Upper Cirrus Layer     |
| 1223-1236     | 7.4-7.6               | $0.051 \pm 0.019$                      | 0.105  | $0.17 \pm 0.06$   | Altocumulus            |
| 1237-1245     | 7.6-7.9               | $0.038 \pm 0.019$                      | 0.034  | $0.088 \pm 0.04$  | Glaciating Altocumulus |
| 1310-1317     | 6.6-7.5               | $0.024 \pm 0.015$                      | 0.019  | $0.22 \pm 0.05$   | Ice Virga              |
| 1310-1330     | 9.5-11.0              | $0.023 \pm 0.013$                      | 0.003  | $0.077 \pm 0.036$ | Upper Ice Cloud        |
| 1318-1356     | 7.0-7.9               | $0.044 \pm 0.017$                      | 0.110  | $0.42 \pm 0.14$   | Altocumulus and Virga  |

ORIGINAL PAGE IS  
OF POOR QUALITY

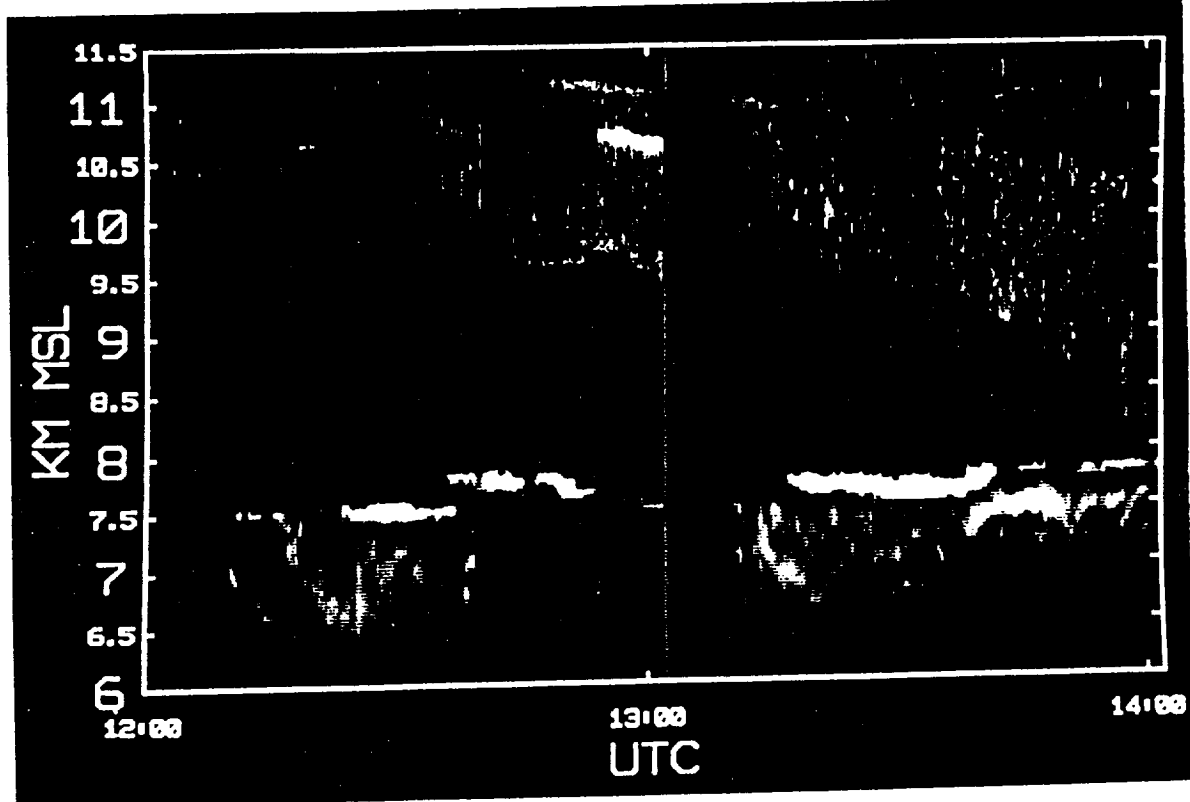
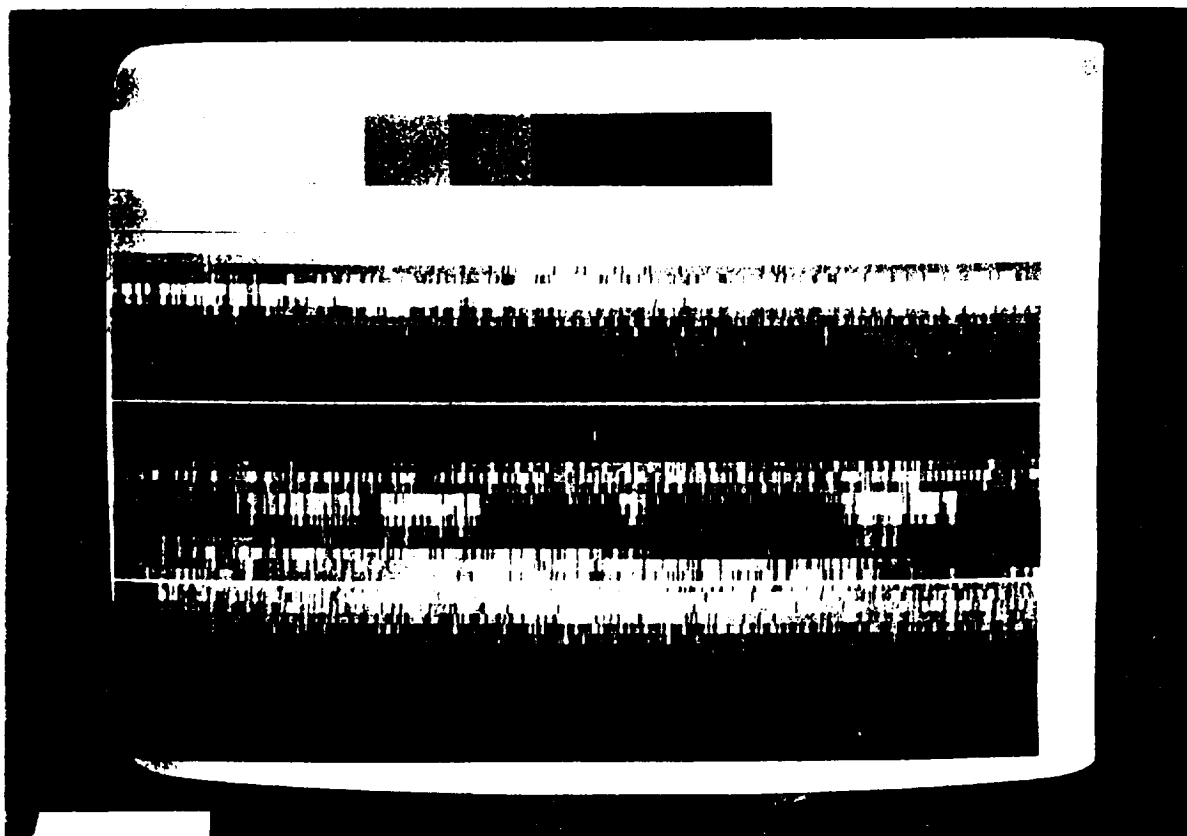


Fig. 14 Expanded gray-scale image of relative laser backscattering (as in Fig. 2) obtained by the Madison HSRL during the period altocumulus were observed within the lidar array. The appearance of the clouds from 7.5 to 8.0 km suggests liquid altocumulus and ice crystal virga, which are also indicated by the corresponding BSPF values given in Table 2.

Fig. 15 HTI display of relative returned signal (in logarithmic units) from the Oshkosh WPLD for 1525-1531 on 28 October, where the horizontal lines are at 5.0 km intervals. Since single shot data is represented, speckle-induced signal fluctuations are apparent. Note that the low altitude signals represent surface aerosol material.



ORIGINAL PAGE IS  
OF POOR QUALITY

ORIGINAL PAGE IS  
OF POOR QUALITY

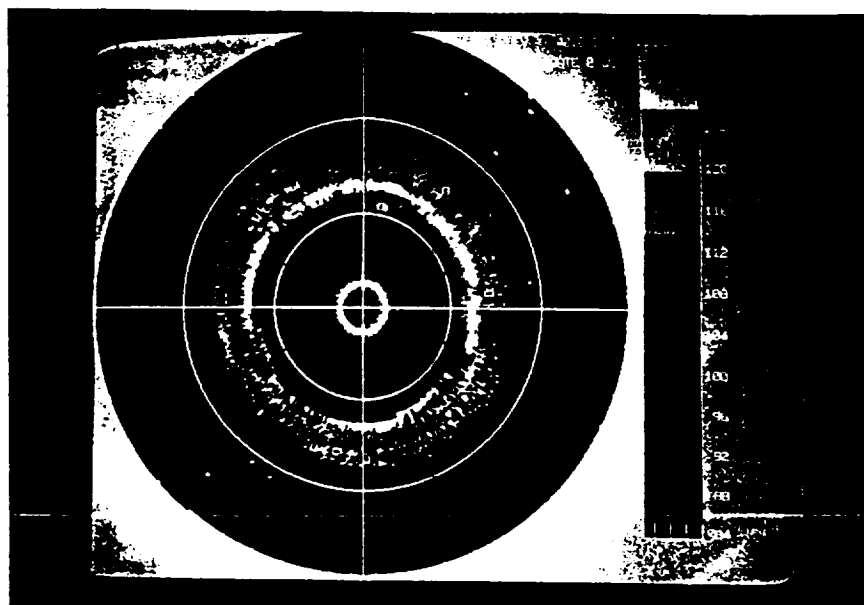


Fig. 16 PPI display of relative returned signals for a  $40^\circ$  elevation angle from the Oshkosh Doppler lidar showing the broken structure of cirrus cloud layers at 1609 on 28 October. The relatively dense lowest layer appears to have largely obstructed the returns from the higher clouds in the northern hemisphere. Each range circle is 10.0 km in radius.

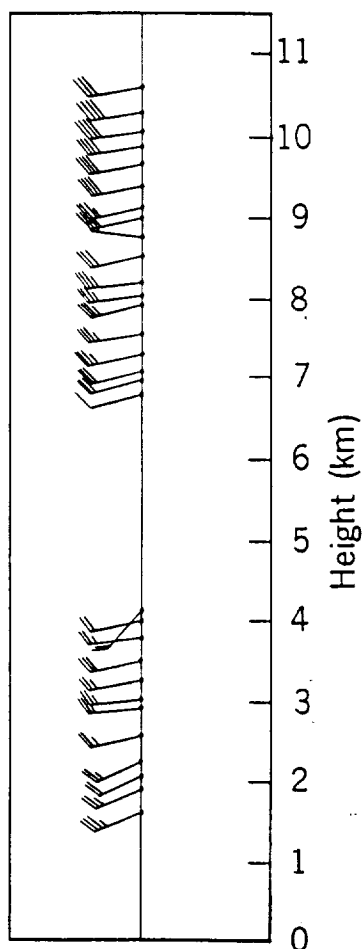


Fig. 17 Wind profile derived from the Doppler measurements of Fig. 16 using the VAD technique. Generally west-southwesterly flow is indicated in the lower tropospheric aerosol and higher cirrus cloud layers.



ORIGINAL PAGE IS  
OF POOR QUALITY

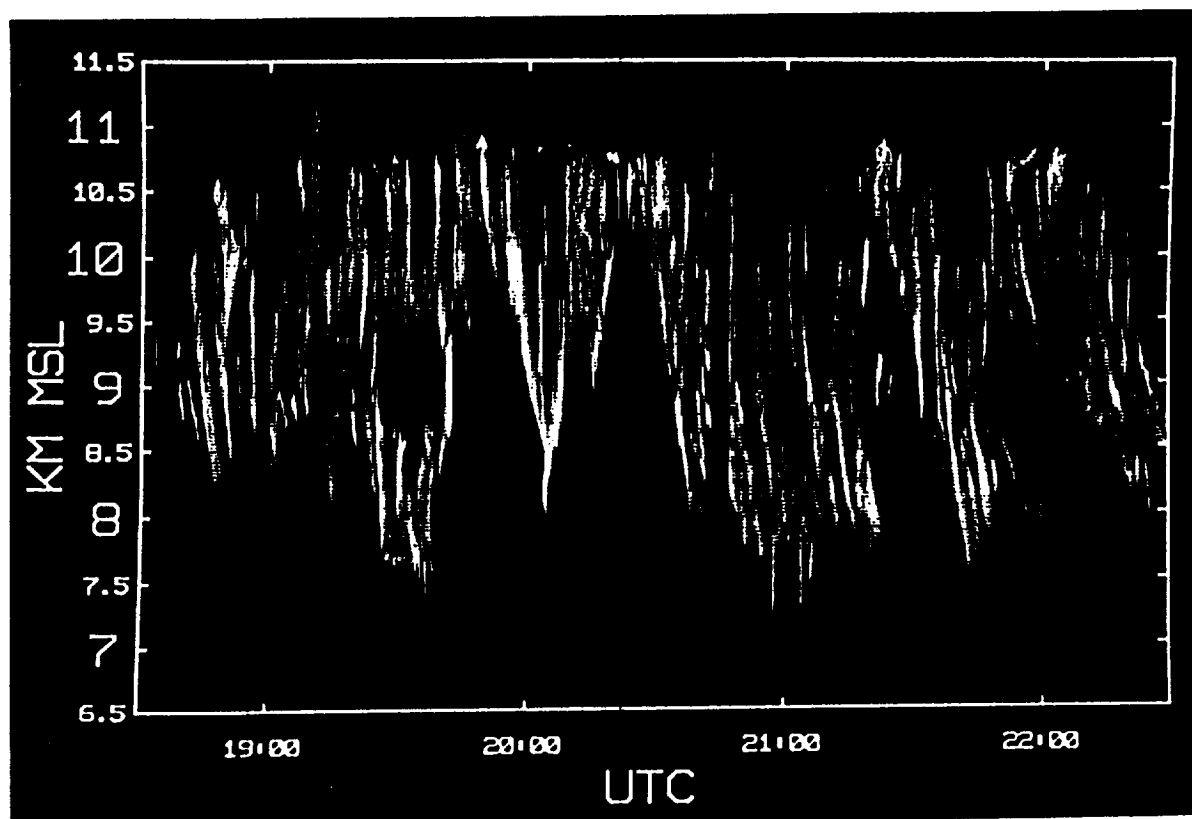


Fig. 18 Expanded gray-scale HTI display of relative laser backscatter (as in Fig. 2) showing the periodic passage of mesoscale cirrus generating regions over the Fort McCoy lidar late on the 28th of October.

ORIGINAL PAGE IS  
OF POOR QUALITY

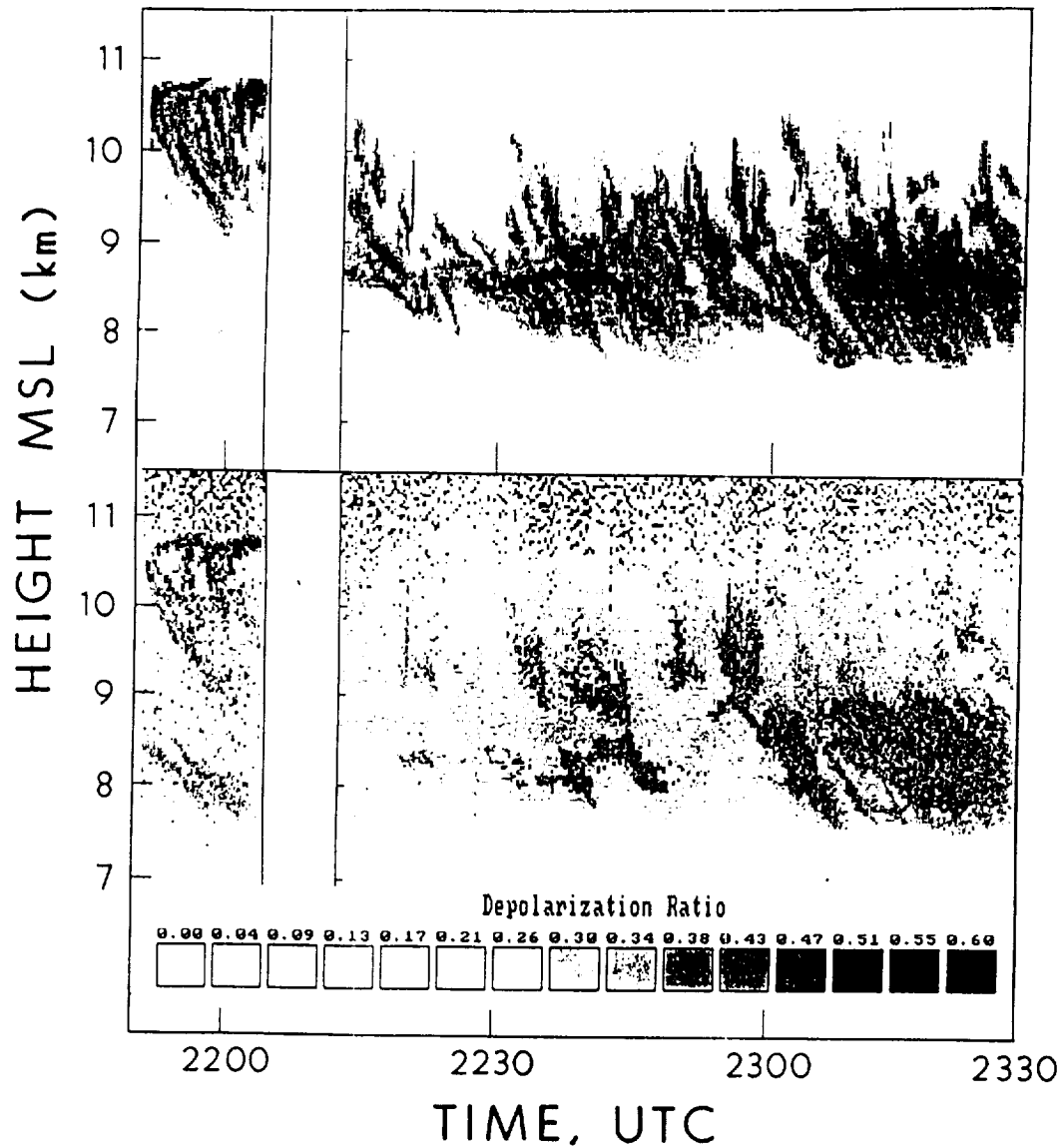


Fig. 19 Expanded gray-scale displays of (a) relative laser backscattering in logarithmic units and (b)  $\delta$  values (note key) for the period following that shown in Fig. 18, in which a more continuous progression of cloud top generating cells and fallstreaks is apparent.

Operations were also restricted by stratocumulus clouds at Oshkosh from ~2030 to 2200. Doppler data show that the appearance of the stratocumulus was associated with the emergence of a relatively strong low level wind maximum from the southwest. (Considerably enhanced aerosol backscattering extending upward to the stratocumulus cloud base was concurrently observed, as can be seen in the lower right corner of Fig. 12a.) Observations that penetrated the low clouds reveal only rather thin cirrus from ~9.5 to 11.0 km until about 2230, when considerably thicker cirrus clouds were probed over Oshkosh.

Although there is no evidence from any of the lidars for cloud generation at the ~8.0 km altitude attributed earlier to the presence of altocumulus, there are indications of occasional enhanced cirrus cloud growth between 8.5 and 9.0 km in Figs. 18 and 19 (see also Starr and Wiley 1990).

## 5. Conclusions

This case study from the 1986 Wisconsin FIRE IFO project provided the participating lidar investigators the opportunity to study a variety of cirrus cloud types, ranging from subvisual to dense, attenuation-limiting cirrus clouds. Over the study period, the crest of an upper level ridge approached and then crossed over the project area. Consequently, although cirrus clouds were initially dissipating in central and southern Wisconsin in the northwesterly flow ahead of the ridge axis, cirrus cloud activity greatly increased during 28 October. According to satellite imagery (Starr and Wiley 1990), a considerable amount of cirrus cloud organization and development occurred within the ground-based lidar array after about 1200 on the 28th as the ridge crest entered the project area. Fortunately, minimal interference to the ground-based observations was caused by low and middle level clouds, although the deepest cirrus cloud structure studied was accompanied by variable altocumulus clouds at ~8 km and stratus clouds at ~4 km, indicating a considerable depth to the dynamical processes responsible for the formation of the cirrus.

The action of several important cirrus generation mechanisms can be discerned in the lidar datasets. The dominant mechanism involved ice particle production in approximately cloud top generating regions, from which trailed sheared particle fallstreaks. Although the formation of ice crystal fallstreaks from the cirrus uncinus cell head has been studied for a considerable time (e.g., Ludlam 1956; Harimaya 1968; Heymsfield 1975), it has only been recently that the importance of mesoscale complexes of cirrus uncinus for large-scale cirrus growth has been illustrated (Sassen et al. 1989a). The physical scales of the generating regions observed here varied from the ~1 km scale of single cirrus uncinus cells through a range of mesoscale uncinus complexes (MUC) up to ~120 km in width. In the more optically dense fallstreaks produced by vigorous generating regions of from a few to several kilometers dimension, inferred particle terminal velocities of  $\sim 1 \text{ m s}^{-1}$  indicate the production of aggregates probably composed of bullet rosette crystals (see Heymsfield et al. 1990). Often a more or less horizontally continuous cirrus cloud base appeared to be defined by successions of strongly sheared fallstreaks. At other times, the cirrus grew downward through sporadically acting precipitation processes, yielding serrated virga patterns trailing from the generation level.

An exceptional high-resolution image of an isolated MUC ~3-4 km in depth was obtained. This structure, a cloud band ~120 km across, contained concentrations of cell complexes embedded not only near cloud top, but also deep

within the precipitation trail. On the basis of cirrus cloud modeling (Starr and Cox 1985) and observational (Sassen et al. 1989a) studies, the cirrus growth within the precipitation trail appears to represent another type of generating mechanism that is triggered by dynamical processes connected with the evaporation of particles into dry subcloud air.

No doubt, this regeneration mechanism, contingent on precipitation, acted at various times during the development of the cirrus, but another important and yet apparently unrecognized mechanism has been identified. This involves the incorporation of supercooled liquid altocumulus and associated virga into deepening cirrus layers. We note that on the basis of several other case studies from the IFO campaign, this coupling of cloud types is by no means unique to the occurrence described here. In the absence of cirrus particle precipitation into the water saturated layer, cellular altocumulus clouds were often observed at temperatures between  $-30^{\circ}$  and  $-35^{\circ}\text{C}$  during the development of a  $\sim 5$  km deep cirrostratus. The thin liquid layers sometimes became glaciated, perhaps in response to ice particle "seeding" from aloft, but were also observed to rapidly dissipate in the presence of active precipitation. In one instance, depolarization data indicate that ice crystals sedimenting from the cirrus aloft became rimed during altocumulus dissipation. Overall, the altocumulus clouds contributed to producing a more horizontally uniform cirrus cloud base, but also persisted at times while embedded well above cloud base in apparently diffuse cirrostratus. Not only the microphysical properties, but also the visible and infrared radiative properties of this deep cirrus cloud were modified, perhaps significantly, by the presence of these liquid cloud layers (see Sassen et al. 1985).

Finally, as particularly evident in the airborne lidar records, the cirrus cloud systems were frequently capped by a thin, but often strongly scattering cloud layer. Although these layers sometimes produced long sheared particle fallstreaks indicative of rather small ice particles, often they produced no virga and consisted of closely spaced shallow cells resembling Kelvin-Helmholtz wave structures. Depolarization data indicate that horizontally oriented plate crystals, or perhaps spherical particles were sometimes present. The dissimilar characteristics of the thin capping layers may have been influenced by radiative effects on the content of the cloud in this elevated region.

In addition to examining some fundamental properties of cirrus clouds, this unique multiple lidar view of a variety of cirrus cloud types will hopefully contribute to the goals of the FIRE IFO project by providing basic cirrus cloud measurements for comparison to those derived from ground-based, airborne, and satellite passive remote sensing experiments. We are gratified that several companion papers have already begun this undertaking.

## References

- Grund, C. J., and E. W. Eloranta, 1990: The 27-28 October 1986 FIRE IFO case study: Cloud optical properties determined by high spectral resolution lidar. Mon. Wea. Rev., 117, (in press).
- Hall, F. F., R. E. Cupp, and S. W. Troxel, 1983: Cirrus cloud transmittance and backscatter in the infrared measured with a CO<sub>2</sub> lidar. Appl. Opt., 27, 2510-2516.
- Harimaya, I., 1968: On the shape of cirrus uncinus clouds: A numerical computation. Studies of cirrus clouds, Part III. J. Meteor. Soc. Japan, 46, 272-279.
- Heymsfield, A. J., 1975: Cirrus uncinus generating cells and the evolution of cirriform clouds. Part III: Numerical computations of the growth of the ice phase. J. Atmos. Sci., 32, 820-830.
- Heymsfield, A. J., K. M. Miller and J. D. Spinhirne, 1990: The October 27-28, 1989 FIRE cirrus case study: Cloud structure and composition from in situ measurements. Mon. Wea. Rev., 117, (in press).
- Kinne, S., T. P. Ackerman, A. J. Heymsfield, F. P. J. Valero, K. Sassen and J. D. Spinhirne, 1990: Cirrus microphysics and radiative transfer: Cloud field study on October 28th, 1986. Mon. Wea. Rev., 117, (in press).
- Ludlam, F. H., 1956: The forms of ice clouds: II. Quart. J. Roy. Meteor. Soc., 82, 257-265.
- Platt, C. M. R., 1979: Remote sounding of high clouds. Part I: Calculation of the visible and infrared optical properties from lidar and radiometer measurements. J. Appl. Meteor., 18, 1130-1143.
- Platt, C. M. R., N. L. Abshire and G. T. McNice, 1978: Some microphysical properties of an ice cloud from lidar observations of horizontally oriented crystals. J. Appl. Meteor., 17, 1220-1224.
- Platt, C. M. R., and K. Bartusek, 1974: Structure and optical properties of some middle-level clouds. J. Atmos. Sci., 31, 1079-1088.
- Platt, C. M. R., J. C. Scott and A. C. Dilley, 1987: Remote sounding of high clouds. Part VI: Optical properties of midlatitude and tropical cirrus. J. Atmos. Sci., 44, 729-747.
- Post, M. J., 1984: Aerosol backscattering profiles at CO<sub>2</sub> wavelengths: The NOAA data base. Appl. Opt., 15, 2507-2509.
- Sassen, K., 1978: Air-truth lidar polarization studies of orographic clouds. J. Appl. Meteor., 17, 73-91.
- Sassen, K., K. N. Liou, S. Kinne and M. K. Graffin, 1985: Highly supercooled cirrus cloud water: Confirmation and climatic implications. Science, 227, 411-413.

- Sassen, K., D. O'C. Starr and T. Uttal, 1989a: Mesoscale and microscale structure of cirrus clouds: Three case studies. J. Atmos. Sci., 46, 371-396.
- Sassen, K., M. K. Griffin and G. C. Dodd, 1989b: Optical scattering and microphysical properties of subvisual cirrus clouds, and climatic implications. J. Appl. Meteor., 28, 91-98.
- Shipley, S. T., D. H. Tracy, E. W. Eloranta, J. T. Trauger, J. T. Sroga, F. L. Roesler, J. A. Weinman, 1983: High spectral resolution lidar to measure optical scattering properties of atmospheric aerosols. Part I: Theory and instrumentation. Appl. Opt., 22, 3716-3724.
- Spinhirne, J. D., M. Z. Hansen and J. Simpson, 1983: The structure and phase of cloud tops as observed by polarization lidar. J. Climate Appl. Meteor., 22, 1319-1328.
- Spinhirne, J. D. and W. D. Hart, 1990: Cirrus structure and radiative parameters from aircraft lidar and spectral radiometer observations: October 28, 1986 case study. Mon. Wea. Rev., 117, (in press).
- Starr, D. O'C., and S. K. Cox, 1985: Cirrus clouds. Part II: Numerical experiments on the formation and maintenance of cirrus. J. Atmos. Sci., 42, 2682-2694.
- Starr, D. O'C., and D. P. Wylie, 1990: The 27-28 October 1986 FIRE IFO cirrus cloud study: Meteorology and clouds. Mon. Wea. Rev., 117, (in press).